

Discovering and exploiting active sensing motifs for estimation

Benjamin Cellini¹, Burak Boyacıoğlu¹, Austin Lopez¹, and Floris van Breugel¹

¹Dept. of Mechanical Engineering, University of Nevada, Reno

Corresponding authors:

Benjamin Cellini, bcellini00@gmail.com

Floris van Breugel, fvanbreugel@unr.edu

ABSTRACT

From organisms to machines, autonomous systems rely on measured sensory cues to estimate unknown information about themselves or their environment. For nonlinear systems, carefully selected sensor motion can be exploited to extract information that is otherwise unavailable, i.e. active sensing. Empirical, yet mathematically rigorous, tools are needed to (1) quantify how sensor movement can contribute to estimation performance, and (2) leverage this knowledge to improve state estimates. Here, we introduce “BOUNDS: Bounding Observability for Uncertain Nonlinear Dynamic Systems”, and Python package *pybounds*, which can discover patterns of sensor motion that increase information for individual state variables. Crucially, it is suitable for partially observable nonlinear systems, accounts for sensor noise, and can be applied to either simulated or observed trajectories. We demonstrate BOUNDS through a case study on a flying agent with limited sensors, showing how active sensing can be leveraged to estimate key variables such as ground speed, altitude, and ambient wind direction. Finally, we present a framework to refine sporadic estimates from bouts of active sensing that combines data-driven state and observability estimation from artificial neural networks with model-based estimation, which we call the Augmented Information Kalman Filter (AI-KF). We validate our framework using altitude estimation given GPS-denied data from an outdoor quadcopter flight. Collectively, our work will help decode active sensing strategies and inform the design of estimation algorithms in sensorimotor systems.

Keywords: observability; Fisher information; active sensing; anemosensing; quadcopter

INTRODUCTION

A fundamental challenge for any autonomous agent—organism or robotic system—is to combine and transform incoming sensory cues into estimates of task-relevant variables. For example, pixels measured by a camera over time can be transformed into information about self-motion. In many cases, variables of interest are not linearly related to available sensor measurements or their derivatives, which complicates estimation. Optic flow cues, for instance, encode a nonlinear function of velocity and distance, making decoding either of these two quantities independently a difficult task^{1,2}.

For a moving agent with nonlinear dynamics, sensory cues are shaped by self-motion or independently moving sensors. Therefore, strategically applied sensor motion can help decouple correlated variables and enhance an agent’s ability to perform an estimation task, a process we refer to as *active sensing*. For example, autonomous agents that want to estimate their velocity or distance relative to nearby objects from optic flow can not do so from a stationary camera. Optic flow captures the ratio of velocity-to-distance ($r = v/z$), making it difficult to estimate either one independently. However, by changing velocity with known acceleration, optic flow can be decoupled to estimate both distance³ and velocity⁴ via the chain rule (i.e. $\dot{r} = \dot{v}/z - r\dot{z}$ can be solved for z). In this example, an agent would simply have to accelerate its vision system to apply this basic active sensing principle—a behavior exhibited by animals such as mice⁵ and mantids⁶.

A major barrier to applying active sensing principles is understanding which patterns of sensor movements are most appropriate for decoupling key variables. How can we under-

stand what extra information can be acquired via sensor movements? Existing approaches leverage the dynamical systems concept *observability*, which describes the ability to infer the state variables of a system from the accessible measurements and inputs⁷. Analytical tools exist for making a binary assessment of nonlinear observability of individual state variables^{8,9}. Quantifying observability levels typically relies on measures based on the singular- or eigen- values of the observability matrix or its Gramian^{10,11,12}, which captures the observability of state combinations. Despite recent efforts¹³, existing methods for quantifying observability levels remain poorly suited for isolating individual state observability for high dimensional and/or partially observable nonlinear systems (i.e. systems for which some state variables cannot be estimated), do not offer a physical unit for observability measures, and do not consider the impact of sensor noise. Furthermore, while data-driven observability tools exist¹⁴, there are no established approaches for applying observability tools to experimental data, such as a measured agent trajectory.

Here we introduce a novel computational pipeline—“BOUNDS: Bounding Observability for Uncertain Nonlinear Dynamic Systems”¹—that leverages tools from control and information theory to address these shortcomings. Principally, BOUNDS empirically determines the observability levels of individual state variables and computes how observability changes as sensors move. We extend established methods for empirically calculating an observability matrix (\mathcal{O}) for non-

¹Note: an early version of our pipeline appears in a different preprint¹⁵, which was never submitted for publication. The prior preprint will be updated to focus on the application of BOUNDS to understanding wind estimation in flying insects.

linear systems^{13,16} to work with real trajectory data through a model predictive control framework¹⁷. To take sensor noise properties into account, we calculate the Fisher information matrix (\mathcal{F}) associated with \mathcal{O} ¹⁸, i.e. the stochastic observability Gramian¹⁹. We introduce a regularization to invert \mathcal{F} under rank-deficient conditions so that we can apply the Cramér–Rao bound²⁰ on partially observable systems and quantify observability with meaningful units. Iterating our pipeline along a dynamic state trajectory intuitively reveals active sensing motifs. Our approach can answer key questions pertaining to sensorimotor systems, such as:

1. Which state variables can be estimated?
2. Which patterns of sensor motion are helpful?
3. Which sensors are required?

BOUNDS can be used as an analysis tool for measured state trajectories or alternatively as a design tool for robotic systems performing state estimation.

Another significant challenge is how to integrate active sensing and observability information for state estimation. It is neither efficient nor practical to constantly perform sensing movements that are unrelated to non-sensing tasks; it would be more efficient to only perform active sensing as needed^{21,22}. Classical state estimation methods, however, do not consider time-varying observability corresponding to active sensing, especially not for individual state variables²³. How might agents continuously compute a state estimate with only sporadic bouts of active sensing that are not corrupted by periods of low observability?

For nonlinear and/or partially observable systems, model based estimators—for instance, the ubiquitous Kalman filter (KF) framework²⁴—can exhibit instability and an increased sensitivity to noise or initialization in weakly observable dimensions^{25,26,27}. Model-based filters typically rely on an arbitrary initialization “guess” for the state and state covariance that is then incremented based on incoming measurement/inputs. While this approach works well—and will eventually converge to an optimal filter for observable, linear dynamics—there is no guarantee that these filters (including nonlinear extensions EKF and UKF^{28,29,30}) will converge for systems that significantly deviate from linearity and observability assumptions. The critical flaw of iterative estimation schemes applied to nonlinear systems, such as the KF, is that measurement information is only correctly incorporated when the state estimate itself is already accurate. When prior state estimates are inaccurate, information is not efficiently extracted from the measurements, and is effectively lost. Data-driven estimators may be able to circumvent this drawback by accessing an arbitrarily large time window of measurements to directly estimate observable state variables. Such estimators, however, will produce very inaccurate estimates during periods of low observability.

We present a novel state estimation framework that leverages the observability information generated by BOUNDS to stitch together sporadic estimates corresponding to bouts of active sensing. Our framework blends two widely used estimation strategies: the Kalman filter and data-driven feed-forward artificial neural network (ANN) estimators. To combine these two estimators in a statistically meaningful manner, we leverage our BOUNDS framework to learn and assign an estimated

variance to the ANN estimates and incorporate this estimate as an augmented measurement in the Kalman filter. We call this framework the Augmented Information Kalman Filter (AI-KF) because it augments the traditional KF with information derived from a recent time history of measurements. Although our approach has broad applications, we illustrate its utility through a specific active sensing challenge: how a flying agent with limited sensors could employ active movements to estimate key variables pertaining to its own movement (altitude, ground speed) and external variables (ambient wind direction). We show that our AI-KF framework outperforms a traditional Unscented Kalman Filter (UKF) in scenarios with poor initial state or covariance guesses, unmodeled disturbances, and trajectories with brief periods of observability.

RESULTS

To describe our computational pipeline, as well as new scientific discoveries, we have organized this section as follows. First, we provide a step-by-step description of the BOUNDS computational pipeline using [Figure 1](#) as a visual organization of these steps. Second, we introduce a specific case study—state estimation for a flying agent—to showcase the different ways our method can be used to discover active sensing motifs from simulations and data. Finally, we introduce a framework for incorporating knowledge of observability into an estimator to provide continuous estimates across sporadic bouts of active sensing, and again illustrate this approach using our case study.

BOUNDS: Bounding Observability for Uncertain Non-linear Dynamic Systems

1. Determine state variables and collect state trajectory time-series

Consider a discrete time-series state trajectory $\tilde{\mathbf{X}}$ consisting of a sequence of observed state vectors $\tilde{\mathbf{x}}_k$ that describe the movement of an agent or sensor, as well as environmental variables ([Figure 1a](#)). The primary objective is to compute a new time-series that describes the observability of each individual variable $\tilde{x}_{i,k}$ along this trajectory, which can be used to evaluate the efficacy of putative active sensing motifs. All relevant state variables that describe the behavior and environment of the agent must be included, although the coordinates of the state variables can be optionally transformed in *Step 6*. The state trajectory can be simulated for testing hypotheses, or measured from real data to evaluate the observability properties of an agent’s underlying movement patterns.

2. Define a model

Once a collection of state variables is determined, a model of the agent’s dynamics must be defined. In general, a good model accounts for 1) the inputs that control locomotion (e.g. forces and torques) 2) basic physical properties such as mass, inertia, damping, etc., and 3) sensory dynamics that model what an agent is measuring ([Figure 1b](#)). We describe our approach for a system with nonlinear deterministic dynamics, and stochastic measurements as

$$\begin{aligned}\mathbf{x}_{k+1} &= \mathbf{f}(\mathbf{x}_k, \mathbf{u}_k), \\ \tilde{\mathbf{y}}_k &= \mathbf{h}(\mathbf{x}_k, \mathbf{u}_k) + \mathbf{v}_k,\end{aligned}\tag{1}$$

where \mathbf{x}_k is the true state vector representing n state variables, \mathbf{u}_k is the input vector, and $\tilde{\mathbf{y}}_k$ is the measurement vector

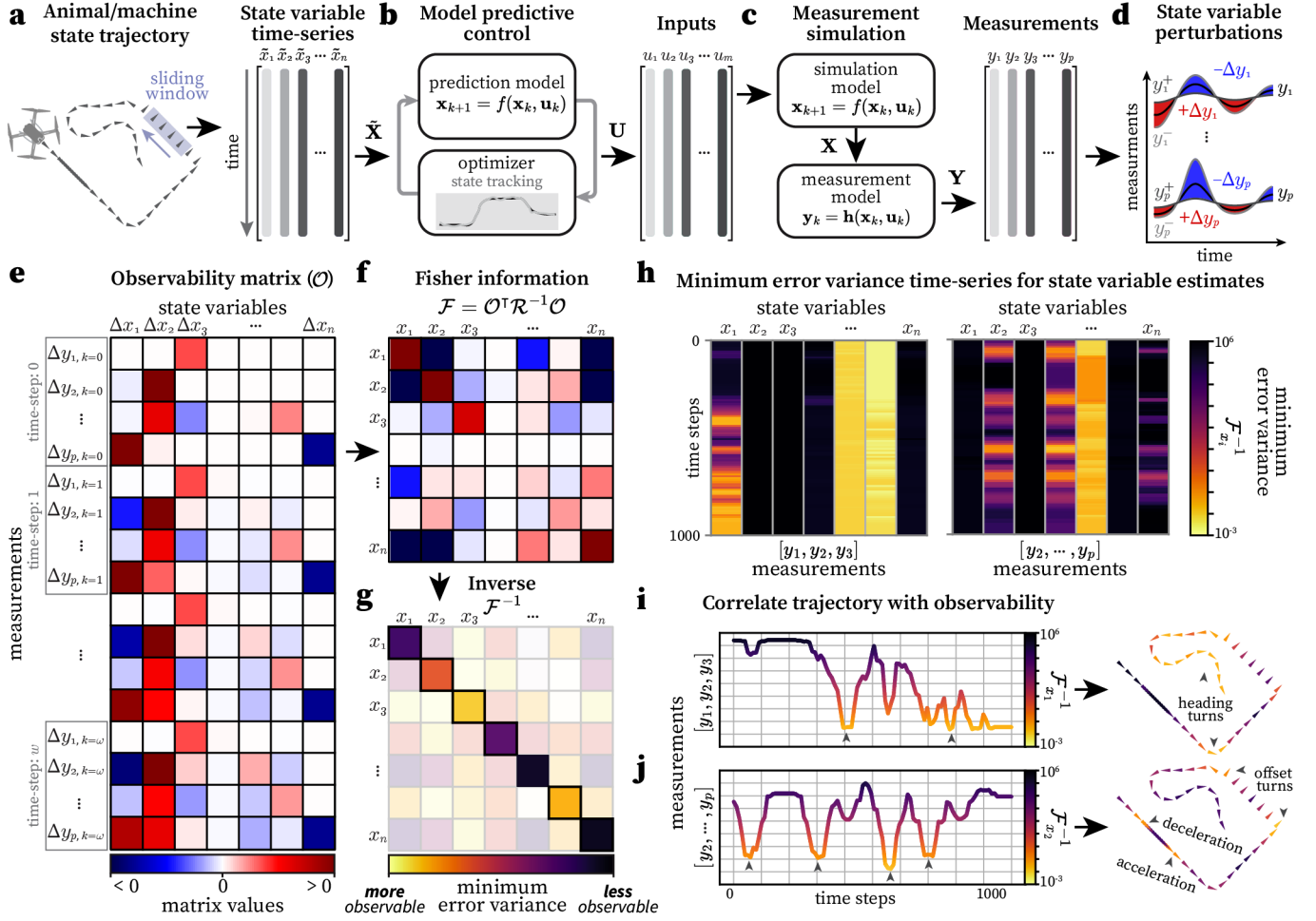


Figure 1. Overview of BOUNDS, a method for discovering active sensing motifs with empirical observability. **a.** A simulated (or measured) state trajectory (in this case, of a flying agent) that is described by a collection of time-series of observed state variables $\tilde{\mathbf{x}}$. **b.** Model predictive control (MPC) is used to find the time-series of control inputs \mathbf{U} required to reconstruct the state trajectory in **a** through a simulation model. **c.** The MPC control inputs \mathbf{U} are used to simulate the dynamics associated with the state trajectory, yielding the nominal reconstructed trajectory \mathbf{X} . A measurement model $\mathbf{h}(\mathbf{x}_k, \mathbf{u}_k)$ simulates the sensor measurements. **d.** Each initial state variable $x_{i,0}$ is perturbed in the positive $x_{i,0}^+$ and negative $x_{i,0}^-$ directions by ϵ . Then the corresponding measurements over time, \mathbf{Y}^{i+} and \mathbf{Y}^{i-} , are computed. The difference between these measurements is used to calculate a numerical Jacobian: $\Delta \mathbf{Y}^i / 2\epsilon$, yielding one column of the observability matrix \mathcal{O} . **e.** An illustration of an observability matrix \mathcal{O} , where the color grid indicates the values in the matrix (corresponding to **d**). The columns indicate the difference of the initial state perturbation $\Delta x_{i,0}$ and the rows indicate the corresponding difference in measurements Δy_k over time for a discrete number of time steps ω . **f.** An illustration of the Fisher information matrix, calculated as $\mathcal{F} = \mathcal{O}^T \mathcal{R}^{-1} \mathcal{O}$, where \mathcal{R} is the block diagonal sensor noise covariance matrix. Colors indicate matrix values as in **e**. **g.** The inverse of the Fisher information matrix \mathcal{F}^{-1} , which encodes the minimum error covariance of the estimate of the state's initial condition \mathbf{x}_0 . The diagonal elements represent the minimum error variance of each individual state variable—inversely correlated with the observability level—where smaller values indicate a higher observability level. **h.** The minimum error variance time-series (normalized units) of all state variables (diagonal of \mathcal{F}^{-1}) over time for the first three sensors $[y_1, y_2, y_3]$ (left) and sensors $[y_2, \dots, y_p]$ (right). Note that some states are persistently observable or unobservable, while other states exhibit time-varying observability, which is dependent on the sensor set. **i.** The minimum error variance time-series of the first state variable x_1 for the first three sensors $[y_1, y_2, y_3]$ (left) and the corresponding correlation with the active sensing motifs in the simulated trajectory (right) from **a**. Time-series corresponds to the first column in **h**. (left). By correlating the time-series with the trajectory, we reveal that only turns in heading improve the observability of x_1 . To make the relationship between temporal patterns in observability and the features of the trajectory more intuitive, we shift the time series back in time by half of the sliding window length, $\omega/2$. **j.** Same as **i** but for state variable x_2 and sensors $[y_2, \dots, y_p]$. Corresponds to the second column in **h** (right). This sensor set renders acceleration/deceleration and turns offset to heading observable, but headings turns have no effect.

corresponding to p measurements at time step k . The function $\mathbf{f}(\mathbf{x}_k, \mathbf{u}_k)$ describes the system dynamics. The function $\mathbf{h}(\mathbf{x}_k, \mathbf{u}_k)$ describes the measurement dynamics, and \mathbf{v}_k is zero-mean additive Gaussian noise with covariance matrix \mathbf{R}_k . The effect of the noise on observability is taken care of in *Step 5*. *Steps 3-4* only use the deterministic measurement equation

$\mathbf{y}_k = \mathbf{h}(\mathbf{x}_k, \mathbf{u}_k)$. A benefit of our empirical approach is that the model does not have to be closed-form, and can instead be a simulation, computational, or data-driven model^{31,12}—for instance, a physics engine model of *Drosophila*³² or finite element model of a flapping wing³³. The only requirement is the ability to simulate the system forward in time.

3. Reconstruct state trajectory through model predictive control

Next, our method applies model predictive control (MPC)³⁴ to find the inputs \mathbf{U} required to reconstruct the state trajectory with the chosen model (Figure 1b). This step is critical for nonlinear or time-varying models where observability can change as a function of the state and input values. The MPC determined inputs are used to simulate the nominal trajectory \mathbf{X} (which should be very similar to the observed trajectory $\tilde{\mathbf{X}}$) and associated measurements \mathbf{Y} (Figure 1c).

4. Construct observability matrix

To quantify the observability of individual state variables, we next compute the observability matrix \mathcal{O} empirically. \mathcal{O} principally encodes information about the sensitivity of the sensor measurements \mathbf{y}_k to small changes in an initial state \mathbf{x}_0 . It can be compactly represented in discrete-time as the Jacobian of the measurements over time with respect to the initial state, $\Delta \mathbf{Y}_\omega / \Delta \mathbf{x}_0$ ³⁵. Here we use \mathbf{Y}_ω to denote the collection of p measurements for each time step from $k = [0 : \omega - 1]$. Following established methods^{31,12}, we empirically approximate the Jacobian by applying small perturbations to each initial state variable $x_{i,0}$, one at a time, in the positive $x_{i,0}^+$ and negative $x_{i,0}^-$ directions. We simulate the system using the inputs \mathbf{u}_k calculated in step 3 (they are not recalculated for the perturbed trajectory), and then compute the difference in the corresponding change in sensory measurements over time $\Delta \mathbf{Y}_\omega^i = \mathbf{Y}_\omega^{i+} - \mathbf{Y}_\omega^{i-}$ (Figure 1d). The end result for each state perturbation is a column vector of length $p \times \omega$, corresponding to p measurements over ω time steps. Repeating these steps for each state variable and stacking the resulting column vectors side-by-side yields the full empirically determined Jacobian, $\Delta \mathbf{Y}_\omega / \Delta \mathbf{x}_0$, which is equivalent to the empirical observability matrix \mathcal{O} (Figure 1e).

5. Compute the Fisher information matrix and its inverse

To compute observability levels for individual state variables in physically interpretable units, we construct the Fisher information matrix as

$$\mathcal{F} = \mathcal{O}^\top \mathcal{R}^{-1} \mathcal{O}, \quad (2)$$

where \mathcal{R} is a block diagonal matrix of the measurement noise covariance matrices at each time step. For the deterministic dynamics we consider, the process noise Q is 0 (see Methods) (Figure 1f)^{36,37}. The Fisher information matrix captures the amount of information that a known random variable, in our case the measurements \mathbf{Y}_ω , carries about unknown parameters, in our case the initial state \mathbf{x}_0 . The Cramér–Rao bound states that the inverse of the Fisher information matrix \mathcal{F}^{-1} sets the lower bound on the error covariance of the state estimate²⁰. Thus, the diagonal elements of \mathcal{F}^{-1} tell us the minimum possible variance in the error for each state variable (for any estimator), inversely correlating with observability (Figure 1g).

In cases where there is at least one unobservable state variable, \mathcal{F} will not be invertible. Therefore, to compute \mathcal{F}^{-1} we add a small regularization term to ensure invertibility³⁸:

$$\mathcal{F}^{-1} = \lim_{\lambda \rightarrow 0^+} \tilde{\mathcal{F}}^{-1} = \lim_{\lambda \rightarrow 0^+} [\mathcal{F} + \lambda I_{n \times n}]^{-1}. \quad (3)$$

For unobservable state variables, this “Chernoff inverse” yields infinity in the corresponding diagonal elements, whereas the

more traditional Moore–Penrose inverse³⁹ yields misleading values. For computational efficiency, we use a small real value for λ , which places an upper bound on the minimum error covariance. Thus, λ must be chosen carefully, so as not to inject too much “artificial” observability into the system, while still allowing an inverse to be computed (see Methods).

6. Perform coordinate transformation

The coordinates of both \mathcal{O} and \mathcal{F} are principally defined in the state space \mathcal{X} , which means that \mathcal{F}^{-1} only provides information with respect to the individual state variables in \mathbf{x} . However, in many cases, it is beneficial to evaluate observability in a set of new coordinates \mathbf{z} . For instance, a system may be defined in Cartesian coordinates, but the polar representation of the state may be the most relevant for observability analysis. The system itself could be redefined in the new coordinates $\mathbf{f}(\mathbf{z}_k, \mathbf{u}_k)$ and the observability analysis pipeline could be repeated. However, this is often tedious for complex systems, not computationally efficient, and is not practical for numerical solvers that rely on a specific coordinate frame. We incorporate a simple method to transform the coordinates of \mathcal{O} (or \mathcal{F}) from an arbitrary state space coordinate basis \mathbf{x} to a new basis \mathbf{z} that bypasses these drawbacks and can be appended post hoc after computing \mathcal{O} with respect to \mathbf{x} .

First, the new basis \mathbf{z} is defined as a transformation of \mathbf{x} such that $\mathbf{z} = T(\mathbf{x})$, where $T(\mathbf{x})$ is a diffeomorphism that preserves the original information content in \mathbf{x} ⁴⁰. Because \mathcal{O} fundamentally represents the Jacobian $\frac{\partial \mathbf{Y}}{\partial \mathbf{x}}$ in continuous time or $\frac{\Delta \mathbf{Y}}{\Delta \mathbf{x}}$ in discrete time, we can compute a coordinate transformation as the Jacobian of \mathbf{x} with respect to \mathbf{z} , evaluated at the initial state \mathbf{x}_0

$$\left. \frac{\partial \mathbf{x}}{\partial \mathbf{z}} \right|_{\mathbf{x}=\mathbf{x}_0} = \left(\left. \frac{\partial T(\mathbf{x})}{\partial \mathbf{x}} \right|_{\mathbf{x}=\mathbf{x}_0} \right)^{-1} \quad (4)$$

and transform the coordinates as

$$\mathcal{O}_z = \left. \frac{\partial \mathbf{Y}}{\partial \mathbf{z}} \right|_{\mathbf{x}=\mathbf{x}_0} = \left. \frac{\partial \mathbf{Y}}{\partial \mathbf{x}} \frac{\partial \mathbf{x}}{\partial \mathbf{z}} \right|_{\mathbf{x}=\mathbf{x}_0} = \mathcal{O}_x \left. \frac{\partial \mathbf{x}}{\partial \mathbf{z}} \right|_{\mathbf{x}=\mathbf{x}_0}. \quad (5)$$

In practice, J_T can be computed numerically or symbolically and evaluated at the initial state \mathbf{x}_0 considered by \mathcal{O} . In some cases, it may be necessary to perform multiple coordinate transforms to evaluate the observability of new state variables that may not jointly satisfy the diffeomorphism/information requirement in a single state space.

7. Reveal active sensing motifs by correlating state dynamics with observability

Finally, we repeat Steps 1–6 in sliding time windows, that is, we use the same window size ω but with initial conditions that start progressively later in time along the nominal trajectory. For each window, we construct \mathcal{O} and \mathcal{F} , optionally perform a coordinate transform, and calculate the minimum error variance for each state variable from $\tilde{\mathcal{F}}^{-1}$. This yields a time-series of minimum error variance along the state trajectory (Figure 1h–Figure 1j), which allows us to evaluate the temporal patterns of observability as a function of state variables and available sensory measurements.

In a toy example for the state trajectory in Figure 1a, we can see that changes in heading angle lead to an order of magnitude decrease in the minimum error variance—equivalent

to an increase in observability—for the first state variable x_1 , compared to a straight trajectory (Figure 1i, Figure 1h). This result is based on measurements from three sensors $[y_1, y_2, y_3]$. However, different observability patterns emerge when considering other state variables and sensor combinations.

For instance, the second state variable x_2 is observable during acceleration/deceleration and turns offset to the heading angle, but requires sensors y_2 to y_p , and does not require sensor y_1 (Figure 1j, Figure 1h). This illustrates that active sensing motifs can be tuned to the sensory measurements that are available and the state variable of interest. A critical point is that each state variable can have different observability properties, and thus distinct active sensing motifs. This approach allows us to investigate fundamental relationships between state variables, sensors, and active sensor motion.

Discovering active sensing motifs in a flying agent

To illustrate the applications of BOUNDS for identifying active sensing motifs, we apply it to a 3D model of a quadcopter drone flying in the presence of ambient wind (see Methods). The primary state variables consist of the agent's attitude (roll ϕ , pitch θ , yaw ψ), translational velocity (v_x, v_y, v_z) in the body-level frame, altitude (z), and ambient wind speed (w) and direction (ζ). We assume the agent has an air flow sensor measures the apparent air flow speed (a) and direction (γ) and an accelerometer that measures the acceleration magnitude (q) and direction (ν). We also assume the agent has a vision system that can measure ventral optic flow magnitude ($r = g/z$) and direction (β), where the ground speed magnitude is defined as $g = \sqrt{v_x^2 + v_y^2}$. In addition, we assume that our agent has access to its own yaw measurement ψ . These measurements make up different components of the wind vector “triangle” (Figure 2a–Figure 2b) experienced by any flying agent⁸, and pose interesting active sensing questions that can be answered via BOUNDS.

In general, active sensing motifs will correspond to different combinations of state values, and changes in states, that can be reached via control within the state space \mathbf{x} . Therefore, it is best practice to employ a methodical exploration of the state space and identify the regions corresponding to increasing observability. However, for illustrative purposes, we examine a limited set of motifs that can easily be visually identified for a flying agent: 1) acceleration, 2) deceleration, 3) turning while changing heading, 4) turning without changing heading (offset turn), and 5) a small turn through the upwind direction ($\zeta = 0$) (Figure 2c). We then asked which states become more or less observable for these motifs depending on what sensors were available.

We simulated a state trajectory with a sequential combination of these motifs for constant wind and evaluated the observability of each state variable as a function of the trajectory (Figure 2c). For brevity, we focus on the wind direction ζ , altitude z , and ground speed g state variables. Note that g is not in the original state space of our model (see Methods) and required our coordinate transformation step in BOUNDS.

We first considered a sensor set consisting of only angular measurements (heading ψ , course direction β , apparent airflow angle γ). We discovered that only the ambient wind direction state variable could be estimated with these measurements, however a change in heading motif was required

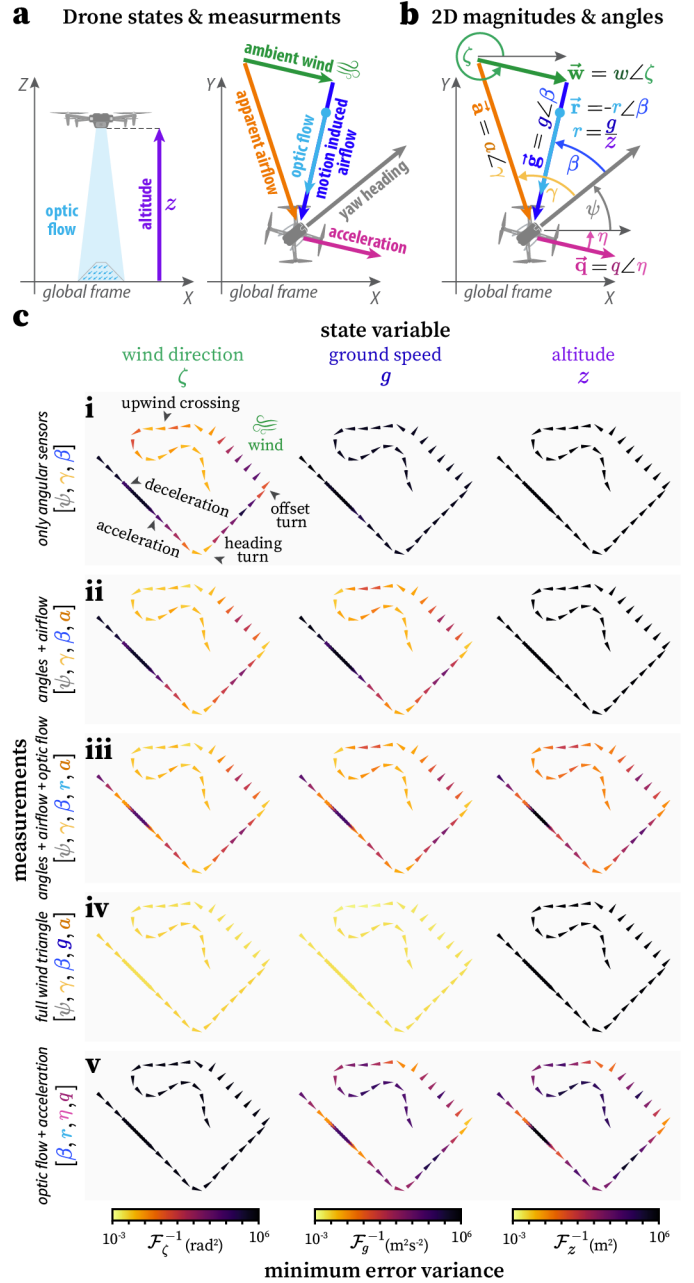


Figure 2. Evaluating putative active sensing motifs. **a.** Illustration of the trigonometric and sensor kinematics of a flying agent in the presence of ambient wind in the XY plane (left) and XZ plane (right). **b.** Each vector quantity in **a** is decomposed into a magnitude and angle, which can be considered separate measurements for observability analysis. **c.** The observability (minimum error variance) of the same simulated flight trajectory for different state variables (columns) and different subsets of measurements from **b** (rows). Observability was calculated for 0.5 s time windows, corresponding to 5 discrete measurements ($\omega = 5$). Note that there are complex interactions between the state variable of interest, the available measurements, and the movement patterns corresponding to an increase in observability.

and straight flight was not sufficient (Figure 2ci). This result is consistent with both analytical observability results⁸ and conclusions from optimal estimator designs⁴¹. A novel finding from our analysis was that larger turns generally led to a higher degree of observability but a small turn passing through

the upwind direction was also adequate for high observability (Figure 2ci). Acceleration/deceleration and offset turn motifs did not markedly increase observability for this sensor set.

Adding a measurement of apparent airflow magnitude (a) made the offset turn sufficient to estimate wind direction and additionally allowed ground speed to be estimated (Figure 2cii). Furthermore, adding an optic flow magnitude measurement (r) made the acceleration/deceleration motifs viable for increasing the observability of wind direction and ground speed, and it rendered the altitude observable (Figure 2ciii).

Replacing the optic flow measurement with a direct ground speed measurement (g) rendered the wind direction and ground speed observable without any motif (even during straight flight), and thus active sensing would not be helpful for this sensor set (Figure 2civ). However, without optic flow this sensor set would not be sufficient to estimate altitude (Figure 2civ).

A sensor set consisting of optic flow magnitude (r) and direction (β) and acceleration magnitude (q) and direction (ν) was suitable for estimating ground speed and altitude during acceleration/deceleration and offset turns (Figure 2cv). However, wind direction was never observable and heading turns had minimal effect on the observability (Figure 2cv).

It is also important to consider the times at which measurements are collected when evaluating active sensing motifs. For some sets of measurements, information must be collected continuously throughout a motif to increase observability (Figure S1a). However, other sets of measurements may allow information to be considered only before and after the motif, with a similar increase in observability to continuously collecting information (Figure S1b). This is an especially important consideration when dealing with systems where sensor noise may be correlated with a motif. For instance, translational optic flow cues may be noisier or less reliable when turning due to the influence of rotational optic flow.

In summary, our approach reveals a diversity of active sensing motifs for a flying agent. We show how an agent would ideally employ distinct movement patterns based on the available measurements and the state variables being estimated. Our results are not particularly sensitive to the model type and generalize well when modeling more complex dynamics (Figure S2). Altogether, these motifs can be used to inform control/estimation strategies and algorithms for autonomous flight with limited sensors. BOUNDS can be applied in a similar manner to any arbitrary system to discover measurement- and movement-dependent sensing motifs.

Observability-informed state estimation

In this section, we present a framework for merging state and observability estimates for agents that rely on active sensing. We focus on four primary steps: 1) training a state estimator, 2) curating training data by observability, 3) training an observability estimator, and 4) observability-informed filtering fusing state and observability estimates. We show an example application of each step for wind direction estimation.

State estimator

We define a state estimator \mathcal{H}_i for any state variable x_i

$$\begin{aligned}\tilde{x}_{i,k} &= \mathcal{H}_i(\mathbf{y}_k, \dots, \mathbf{y}_{k-\omega}, \mathbf{u}_k, \dots, \mathbf{u}_{k-\omega}, \mathcal{R}_{\omega_k}) \\ &= \mathcal{H}_i(\mathbf{Y}_{\omega_k}, \mathbf{U}_{\omega_k}, \mathcal{R}_{\omega_k}).\end{aligned}\quad (6)$$

\mathcal{H}_i is a function that maps the time history of measurements \mathbf{Y}_{ω_k} (and optionally inputs \mathbf{U}_{ω_k} and measurement noise covariance \mathcal{R}_{ω_k}) in the time window ω to the current state estimate $\tilde{x}_{i,k}$ at time step k . Notably, \mathcal{H}_i can consider the entire time window ω of information at once, and is not sensitive to initialization, thus can potentially avoid the pitfalls associated with Kalman filtering. In principle, \mathcal{H}_i could be any function, but we employ a feed-forward artificial neural network (ANN) for its generality, flexibility, and ability to operate without relying on a predefined dynamical model.

We designed a wind direction state estimator ANN using a limited set of angular measurements $[\psi, \gamma, \beta]$ (Figure 3a, Figure S3a–Figure S3b). Our observability analysis tells us that the agent must turn with a change in heading in order for the ANN to yield accurate estimates of wind direction (Figure 2ci).

Curating training data by observability

With a simulation model, or experimental testbed where x_i can be measured directly, one should be able to generate a rich dataset to train and validate a state estimator \mathcal{H}_i . However, the distribution of observability within the training dataset is critical. For instance, attempting to train an estimator on primarily unobservable data—for instance, straight trajectories for our wind direction estimator (Figure 2ci)—will surely lead to poor results. Alternatively, one could leverage prior knowledge of observable motifs to generate high quality training data, or curate a subset of an existing dataset that has an appropriate distribution of observability.

We generated training data by randomly simulating a diversity of trajectories (Figure 3b, see Methods). We ensured that the trajectories densely spanned a large envelope of the state space and yielded a wide distribution of observability values (Figure 3c). We then separated the data into ten equally sized bins, sorted by the observability of wind direction (Figure 3c). This allowed us to train ANN's on inputs with distinct distributions of observability. We specifically performed an analysis of the ANN wind direction estimate error variance $\text{Var}(\zeta - \tilde{\zeta})$ when trained on varying percentages of the training dataset—once when the training data was sorted by observability level, and once when the data was randomly sorted (Figure 3d, Figure S4).

When comparing the observability-sorted to randomly-sorted trained ANN's, we discovered that training on our entire dataset led to worse performance (higher loss) on most of the higher observability data (Figure 3e). Training on only higher observability data was unsurprisingly better for higher observability data, but led to overfitting and worse performance on the low-to-medium observability data (Figure 3e). We found that training on between the 40% and 70% most observable data in our dataset led to the best overall performance of the ANN (Figure 3e). Altogether, we found that sorting data by observability allowed the curation of a smaller, but richer, dataset that can increase ANN performance (Figure 3e). Furthermore, we found that observability was a good predictor of ANN performance and correlated with the ANN error variance (Figure 3f). In theory, an ANN should not be able to outperform the minimum error variance \mathcal{F}_{ζ}^{-1} , but in practice an ANN can learn certain heuristics that are viable within the space of the training data, especially for bounded circular data.

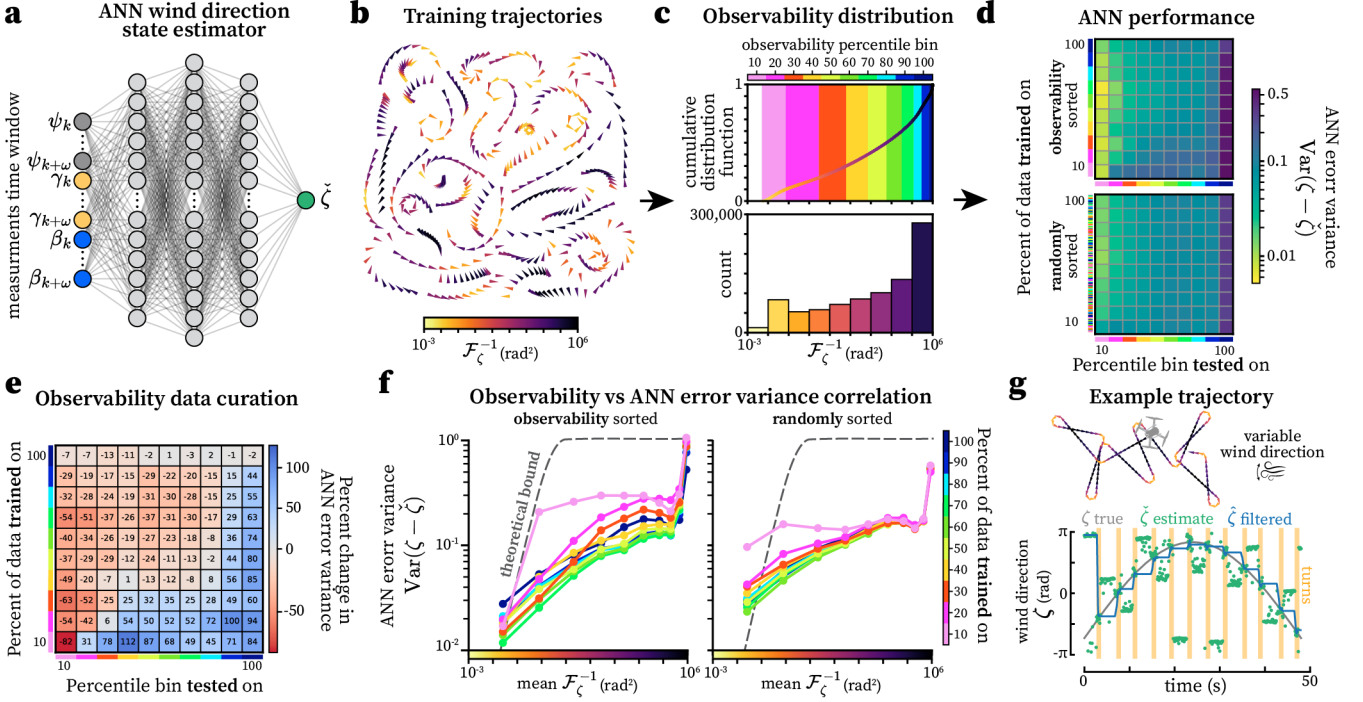


Figure 3. Observability-informed state estimation. **a.** Artificial neural network (ANN) state estimator for wind direction (\mathcal{H}_ζ). Inputs are the yaw heading angle (ψ), apparent wind angle (γ), and course direction angle (β) in the time window ω . **b.** A subset of simulated flying agent trajectories used for training and testing the ANN state estimator. $N = 40,000$ trajectories total. **c.** The distribution (bottom) and cumulative distribution function (top) of wind direction observability (\mathcal{F}_ζ^{-1}) across all training and testing trajectories. **d.** A comparison of the testing error variance for the wind direction state estimator ANN (\mathcal{H}_ζ) when trained on different percentages of the training data—for data sorted by observability (sorted high-to-low, top) and randomly sorted (bottom). The y-axis indicates how much data was used in training, and the x-axis indicates what bin percentile was used to test the ANN (testing data always sorted by observability). **e.** Same as **d.** but showing the relative change in error variance between observability-sorted and randomly sorted training data. Red values (< 0) indicate better performance when sorting by observability. **f.** The mean observability mean(\mathcal{F}_ζ^{-1}) of each bin in the training dataset vs the ANN error variance $\text{Var}(\zeta - \hat{\zeta})$ for ANN's trained on different percentages of the training dataset for observability-sorted (left) and randomly sorted (right) training data. The theoretical bound of the ANN performance is shown as a dashed line (bounded at 1 for circular data). **g.** (top) An example simulated trajectory of a flying agent in the presence of time-varying wind direction. Color along trajectory indicates observability. (bottom) A comparison of true wind direction (ζ), ANN wind direction estimate ($\hat{\zeta}$), and the observability-filtered estimate ($\hat{\zeta}_{\text{filtered}}$). Measurement noise covariance was set to $\mathcal{R} = 10^{-3} I_{p \times p}$.

For instance, when the wind speed is much greater than the ground speed in our flying agent, the wind direction can be approximated as $\zeta \approx \psi + \gamma$, even during unobservable straight flight.

Observability estimator

To know when to expect accurate or inaccurate estimates from \mathcal{H}_i , it is also necessary to know the observability of x_i . However, calculating the true observability $\mathcal{F}_{x_i}^{-1}$ using BOUNDS or other empirical observability tools relies heavily on knowing the full state \mathbf{x}_k in advance. The agent only has access to \mathbf{Y}_{ω_k} , \mathbf{U}_{ω_k} , and \mathcal{R}_{ω_k} , therefore \mathbf{x}_k is not directly available. Even \mathcal{H}_i 's for each state variable could not be relied on to estimate \mathbf{x}_k , unless \mathbf{x}_k was always observable, thus we have a circular problem that does not allow us to compute observability using traditional approaches. In practice, calculating observability online may be impractical, or impossible. However, we take a data-driven approach to solve this problem by constructing an observability estimator \mathcal{G}_i of the form

$$\tilde{\mathcal{F}}_{x_i,k}^{-1} = \mathcal{G}_i(\mathbf{Y}_{\omega_k}, \mathbf{U}_{\omega_k}, \mathcal{R}_{\omega_k}), \quad (7)$$

where $\tilde{\mathcal{F}}_{x_i,k}^{-1}$ is an estimate of the current observability of x_i at time step k . We can similarly use an ANN to construct \mathcal{G}_i —however, for simple active sensing motifs there may be a relationship between a measured movement, e.g. turning, and observability that can be exploited to develop a less complex model. With sufficiently rich training-data, \mathcal{G}_i should produce accurate observability estimates. In some cases, there may be simple observable motifs encoded in \mathbf{Y}_{ω_k} that \mathcal{G}_i can easily learn. However, there may be instances where \mathbf{Y}_{ω_k} simply does not contain enough information to precisely estimate $\tilde{\mathcal{F}}_{x_i}^{-1}$ —therefore, the performance of \mathcal{G}_i should be carefully validated.

We trained a wind direction observability estimator ANN (Figure S3c) using the entire distribution of our training data. For low measurement noise, the estimator was sufficient to estimate the true observability within an order of magnitude and correctly predicted the spikes in observability associated with turns (Figure S3d). However, larger measurement noise led to overestimates (Figure S3d). While it may be possible to improve the ANN sensitivity to measurement noise via improved layer design and training data, estimating observability in high-

noise data will always be a significant challenge because it is difficult to tease apart “good” changes in measurements due to active sensing and “bad” changes due to noise.

Observability-informed filtering

The final step for observability-informed state estimation is to leverage the observability estimate $\tilde{\mathcal{F}}_{x_i}^{-1}$ to adaptively filter the “raw” state estimate $\tilde{x}_{i,k}$. The filtered state estimate $\hat{x}_{i,k}$ should ideally not change too quickly when observability is low and $\tilde{x}_{i,k}$ is inaccurate, but converge quickly to $\tilde{x}_{i,k}$ when observability is high and $\tilde{x}_{i,k}$ is accurate. The simplest approach is to use an adaptive low-pass filter with coefficients that are dynamically scaled by the estimated observability. We propose a simple update equation,

$$\hat{x}_{i,k} = \alpha_k \tilde{x}_{i,k} + (1 - \alpha_k) \hat{x}_{i,k-1}, \quad (8)$$

where $\hat{x}_{i,k}$ is the current filtered estimate of the state x_i , $\hat{x}_{i,k-1}$ is the filtered estimate at the previous time step, and $\tilde{x}_{i,k}$ is the current raw estimate of the state from \mathcal{H}_i (Figure S5). The coefficient α_k is a time-varying weight between 0 – 1 that determines how much to update the current filtered estimate with the current raw estimate. α_k can be determined from an inverted and normalized function of the estimated observability $\tilde{\mathcal{F}}_{x_i,k}^{-1}$.

With validated state and observability estimators (Figure S3), we next applied our observability filter to a testing trajectory with time-varying wind direction, which the ANN’s had not been trained on (Figure 3g). This trajectory was designed to only have sporadic bouts of active sensing (turns) to make estimation more challenging. We also injected sensor noise into the measurements \mathbf{Y}_{ω_k} . As expected, we found that the ANN raw estimate ($\check{\zeta}$) was only accurate during turns (periods of high observability)—in between turns the estimate was consistently offset (Figure 3g). However, the filtered estimate ($\hat{\zeta}$) smoothly and quickly converged to the true value of wind direction (ζ) during a turn (Figure 3g). With sufficiently frequent turns the observability-filtered estimate could track the changing wind direction, although high enough measurement noise did lead to worse performance (Figure S3e–Figure S3g).

Augmented Information Kalman Filter

While the observability-filtering approach we outline is adequate for estimating individual state variables given sufficient bouts of active sensing, it lacks the powerful statistical rigor of model-based methods like the Kalman filter (KF). For instance, the observability-filter essentially acts like a zero-order hold during periods of low observability, but a KF can potentially make use of “dead-reckoning” to track states with reasonable accuracy in these same periods⁴².

Conversely, Kalman filtering comes with its own issues when dealing with weakly observable and nonlinear systems^{25,26,27}. A major issue is that an incorrect guess for the initial state $\hat{\mathbf{x}}_{k=0}$ can drive the new KF estimate in the incorrect direction. Both the new state prediction and innovation terms in the KF update equation,

$$\underbrace{\hat{\mathbf{x}}_{k+1}}_{\text{new state}} = \underbrace{f(\hat{\mathbf{x}}_k, \mathbf{u}_k)}_{\text{predicted state}} + \underbrace{K}_{\text{Kalman gain}} (\underbrace{\tilde{\mathbf{y}}_k - h(\hat{\mathbf{x}}_k, \mathbf{u}_k)}_{\text{innovation}}), \quad (9)$$

rely on an accurate $\hat{\mathbf{x}}_k$, so the KF will struggle to converge. Additionally, the initial state covariance $P_{k=0}$ influences the computation of the Kalman gain K , so a wrong guess for $P_{k=0}$ can also lead to unexpected behavior. For linear and observable systems this is generally not a problem, but when observability is low or sparse in time, and dynamics are nonlinear, a KF filter is far from an optimal estimator. Because only one measurement at a time is used to update the state estimate (Equation 9), if $\hat{\mathbf{x}}_{k=0}$ or P_k was wrong in the past, then potentially useful prior information is lost. Alternatively, an estimator that is able to consider the entire time-history of measurements may be able to outperform a KF.

We present a method augmenting the traditional Kalman filter framework with information from data-driven estimators, which we call the Augmented Information Kalman Filter (AI-KF) (Figure 4a). The AI-KF works by augmenting a KF with extra information from a data-driven state estimator, and then telling the KF when to trust this information more or less with a time-varying noise covariance matrix that is adjusted based on an observability estimate. The main benefit is that the augmented information considers an arbitrarily long time-history of measurements that can make up for a “bad” initialization of the KF. The AI-KF is primarily applicable for nonlinear and partially observable systems that have some state variables with time-varying observability properties.

First, the original Kalman filter measurement vector \mathbf{y} is augmented with a state estimate \tilde{x}_i from a data-driven state estimator \mathcal{H}_i at each time step,

$$\mathbf{y}' = \begin{bmatrix} \mathbf{y} \\ \tilde{x}_i \end{bmatrix}. \quad (10)$$

In principle, the measurement vector can be augmented with any subset of data-driven state variable estimates $\{\tilde{x}_i, \dots, \tilde{x}_n\}$. However, for brevity, we show the process for a single state variable.

Next, the original Kalman filter noise covariance \mathcal{R} is augmented with the noise covariance for the data-driven state estimate \tilde{x}_i

$$\mathcal{R}' = \begin{bmatrix} \mathcal{R} & \text{Cov}(\mathbf{y}, \tilde{x}_i) \\ \text{Cov}(\mathbf{y}, \tilde{x}_i)^\top & \text{Var}(\tilde{x}_i) \end{bmatrix}$$

where \tilde{x}_i is the data-driven estimation error for the state variable x_i . The augmented portion of \mathcal{R}' , which we will refer to as $\tilde{\mathcal{R}}_i$, encodes the covariance of \tilde{x}_i both with itself and all other measurements.

The critical step is constructing $\tilde{\mathcal{R}}_i$ to vary in time based on the accuracy of the state estimate \tilde{x}_i . This can be accomplished multiple ways. If \mathcal{H}_i is efficient, then the augmented portion of \mathcal{R}' is equivalent to the observability from \mathcal{F}^{-1} , which can be estimated with \mathcal{G}_i . However, it is more statistically consistent to construct a covariance function by performing a post hoc analysis of the state estimator \mathcal{H}_i itself to determine the error covariance as a function of the estimator inputs $\tilde{\mathcal{R}}_i(Y_\omega, U_\omega)$. Notably, the off-diagonal elements of $\tilde{\mathcal{R}}_i$ will generally be non-zero because \tilde{x}_i is a function of \mathbf{y}_k (in addition to prior measurements), but the diagonal element $\tilde{\mathcal{R}}_{i,i}$ will generally have the most impact.

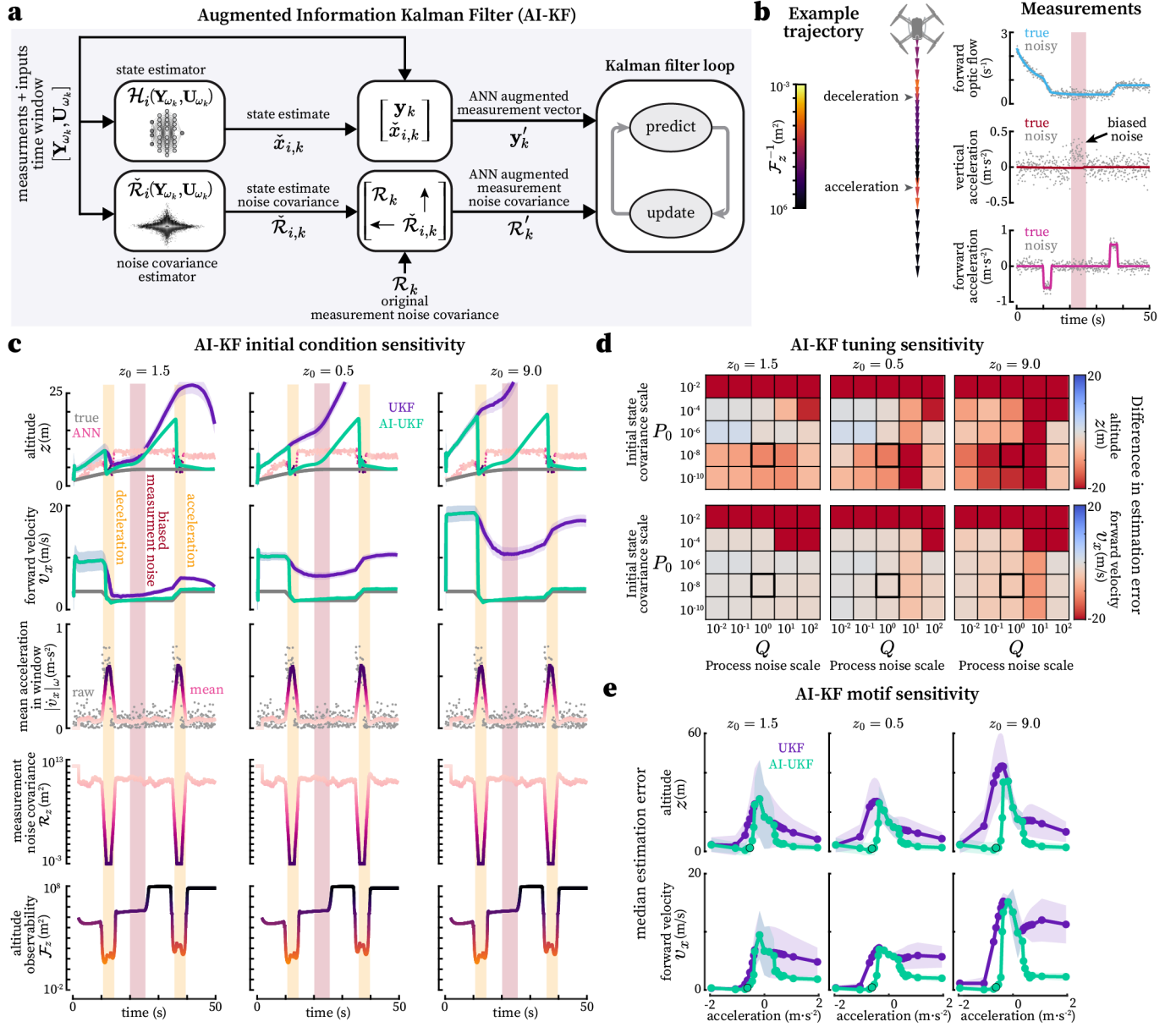


Figure 4. Augmented Information Kalman Filter. **a.** Overview of the Augmented Information Kalman Filter (AI-KF) state estimation framework. The measurement vector \mathbf{y}_k is augmented with a data-driven state estimate $\tilde{\mathbf{x}}_{i,k}$. The corresponding state noise covariance is estimated $\tilde{\mathcal{R}}_{i,k}$ and used to dynamically adjust the full augmented noise covariance matrix \mathcal{R}'_k based on the state estimate accuracy (or observability). **b.** (left) The AI-KF framework is applied to estimate altitude for a simulated trajectory consisting of straight flight with a brief deceleration and sequential acceleration. Altitude is observable during acceleration/deceleration (see Figure 2cv) given measurements of forward optic flow, forward acceleration, and vertical acceleration. (right) Noisy measurements used in our simulation with additive zero-mean Gaussian noise with a variance of 10^{-2} for each measurement. There is also a brief period of biased (nonzero-mean) noise added to the vertical acceleration measurement. **c.** A comparison of an Unscented Kalman Filter (UKF, purple) and Augmented Information Unscented Kalman Filter (AI-UKF, green) state estimation results with varied initial altitude state estimates, for the trajectory in **b**. The shading around the curve insinuates the 2-σ estimate bound. The noise variance of the augmented altitude measurement $\text{Var}(\hat{z})$ (top, pink scaled) was dynamically adjusted proportionally to the mean acceleration magnitude in the time window ω . **d.** A comparison of the median error of the UKF and AI-UKF for varying process noise covariance matrix (Q) scales and varying initial state covariance matrix (P_0) scales for varying values of the initial altitude estimate. The results in **d** correspond to the square with a bold outline. **e.** Comparison of the UKF and AI-UKF median error across different mean accelerations for varying values of the initial altitude estimate. The AI-UKF always performs better or equal to the vanilla UKF. The advantage of the AI-UKF is most pronounced for small but non-zero levels of acceleration.

Applying AI-KF to estimate altitude

We implemented our AI-KF framework for a flying agent to estimate altitude z and forward velocity v_x from only forward ventral optic flow r_x , forward acceleration \dot{v}_x , and vertical acceleration \dot{v}_z (see [Methods](#)). Observability analysis tells us that this estimation problem is solvable given non-zero acceleration ([Figure 2cv](#))³. However, it is a more challenging problem than wind direction estimation (see difference in observability in [Figure 2c](#)) and more clearly illustrates the benefit of the AI-KF. In this example, we augment an Unscented Kalman filter (UKF), which is appropriate for nonlinear dynamics—although our method is applicable to most Kalman filter extensions. We show that the AI-UKF can improve state estimation for both simulated data and real data from an outdoor quadcopter flight.

We used a simplified 2D kinematic model for the AI-UKF with only the state variables altitude (z), vertical velocity (v_z), and forward velocity (v_x)

$$\dot{\mathbf{x}} = \begin{bmatrix} \dot{z} \\ \dot{v}_z \\ \dot{v}_x \end{bmatrix} = \begin{bmatrix} v_z \\ u_z \\ u_x \end{bmatrix}, \quad (11)$$

with the measurement model

$$\mathbf{y} = [r_x] = [v_x/z], \quad (12)$$

where the inputs u_z and u_x are measured accelerations. We chose this model for its simplicity and generality—it should be applicable to virtually any flying agent.

We designed a data-driven ANN estimator that can accurately estimate altitude given a two-second time window of optic flow and forward acceleration measurements ([Figure S6a–Figure S6b](#)). We designed our ANN and training data to assume a constant altitude, thus we did not include the vertical acceleration as an input and left that for the KF to utilize. We augmented the measurement vector with the altitude estimate

$$\mathbf{y}' = \begin{bmatrix} r_x \\ \tilde{z} \end{bmatrix}. \quad (13)$$

Guided by our observability analysis, which revealed that the variance of our altitude estimator should be strongly correlated with lateral acceleration ([Figure S6c–Figure S6d](#)), we constructed a function for the altitude estimate’s noise variance $\tilde{\mathcal{R}}_{z,z}$ based on the empirical relationship between the mean lateral acceleration magnitude in the ANN time window ([Figure S6c–Figure S6d](#)). To match the rapid decline of altitude estimation errors with increasing lateral accelerations we chose a function with a negative exponential form,

$$\tilde{\mathcal{R}}_{z,z} = (\rho_{\min})^{1-\sigma} (\rho_{\max})^{\sigma}, \quad (14)$$

where ρ_{\min} and ρ_{\max} are tunable positive parameters that set the absolute minimum and maximum of $\tilde{\mathcal{R}}_{z,z}$. The exponent σ is a normalized function of the lateral acceleration in the ANN time window given by

$$\sigma = \frac{\max(|\dot{v}_x|) - \text{mean}(|\dot{v}_x|_{\omega})}{\max(|\dot{v}_x|) - \min(|\dot{v}_x|)}. \quad (15)$$

The value of σ can range between $[0, 1]$, ensuring that for windows with lateral accelerations close to the maximum $\sigma = 0$

and ρ_{\min} will dominate, leading to a small value for $\tilde{\mathcal{R}}_{z,z}$, allowing the ANN altitude estimate to have a strong influence on the Kalman filter update equation. For our system, we chose $\rho_{\min} = 10^{-3}$ to allow the accurate augmented altitude measurements have a large influence when acceleration was large, and we set $\rho_{\max} = 10^{12}$ to ensure that periods of low acceleration did not affect the AI-UKF. For simplicity, we set the off-diagonal elements of $\tilde{\mathcal{R}}_z$ to 0. Although a correlation analysis of the ANN estimator may provide the most statistically consistent values for the off-diagonal elements, we go on to show that the AI-KF can be effective without this step.

To test the AI-UKF, we simulated a straight trajectory with a brief (3 sec) deceleration and then brief acceleration ([Figure 4b](#)). We added zero-mean Gaussian measurement noise for the entire trajectory length and a small amount of biased noise between the deceleration and acceleration ([Figure 4c](#)). The brief periods of high observability and unmodeled biased noise combined with nonlinear dynamics make this a prime example for demonstrating the utility of the AI-UKF.

We applied both a UKF and AI-UKF to the trajectory while varying the guess for the initial altitude z_0 ([Figure 4d](#)). We found that the performance of a regular UKF was overall poor ([Figure 4d](#)). For some initial conditions, the UKF altitude estimate moved in the correct direction during the deceleration (first period of high observability) ([Figure 4d](#)). However, the UKF had a hard time fully converging to the true altitude and correcting during the acceleration (second period of high observability) after being thrown off by the biased noise ([Figure 4d](#)). In contrast, the AI-UKF was able to converge quickly and smoothly to the true altitude during both periods of high observability ([Figure 4d](#)). Due to the coupling of altitude and forward velocity in the optic flow measurement ($r_x = v_x/z$), the forward velocity estimate also converged close to the true value for the AI-UKF, but again not for the UKF ([Figure 4d](#)). This illustrates how just a single data-driven estimator may be needed to estimate correlated state variables via the AI-KF.

We also performed a sensitivity analysis to understand how the choice for the initial covariance $P_{k=0}$ and tuning of the process noise covariance matrix Q affected the relative performance of the AI-UKF compared to the UKF. We specifically compared the median error after the first acceleration for the UKF and AI-UKF ([Figure 4e](#)). We found that the AI-UKF consistently outperformed the UKF ([Figure 4e](#)). While it may be possible to choose a specific combination of $x_{k=0}$, $P_{k=0}$, and Q for a regular UKF that approximately matches the AI-UKF performance, there is not a universal choice that will work on all trajectories and initializations ([Figure 4e](#)). Therefore, the AI-UKF provides a degree of robustness to these initialization and hyperparameter choices.

Another important consideration is that the amount of observability, or amount of acceleration/deceleration in this case, will influence the advantage of the AI-UKF. To test the generality of the AI-UKF, we applied it to a range of simulated trajectories with varying accelerations and found that the AI-UKF consistently matched or exceeded the performance of the UKF ([Figure 4f](#)). In general, for large enough accelerations/decelerations, both the UKF and AI-UKF performed equally well ([Figure 4f](#)). However, the UKF struggled with smaller accelerations/decelerations, while the AI-UKF was

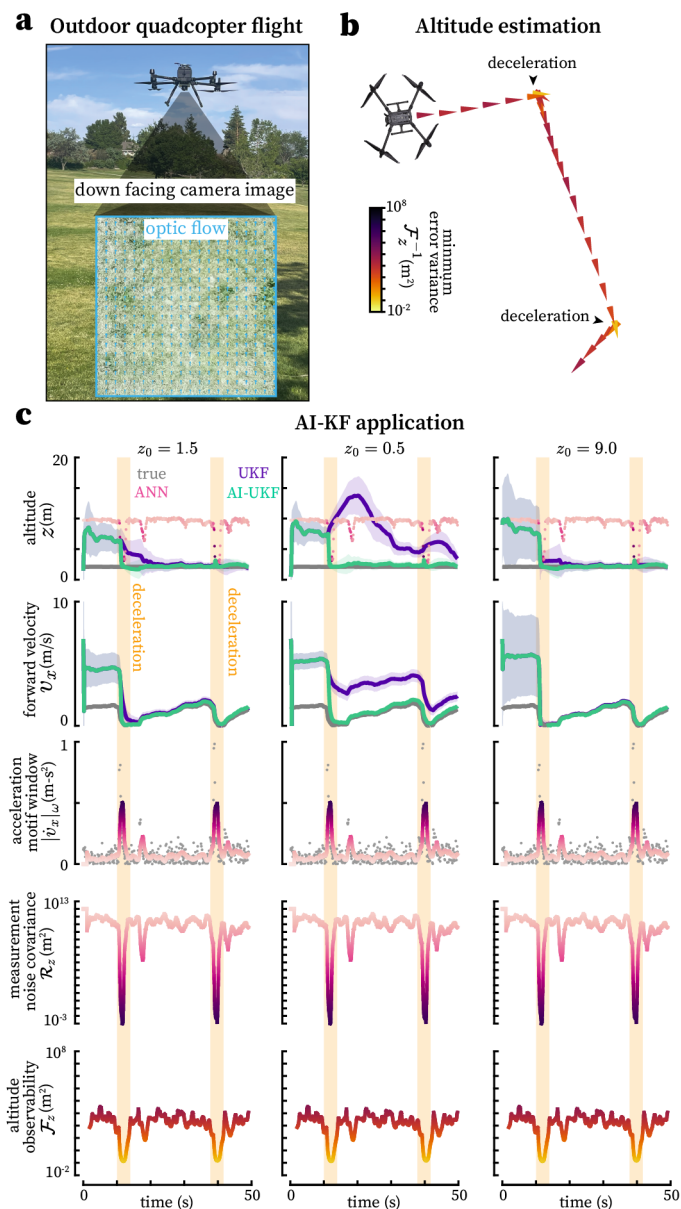


Figure 5. Augmented Information Kalman Filter application for outdoor quadcopter flight. **a.** Quadcopter (DJI Matrice 300 RTK) flying in an outdoor environment with a representative ventral camera image and computed optic flow vectors. **b.** An experimental measured quadcopter trajectory with estimated altitude observability computed using the approach in Figure 1, illustrating how our BOUNDS framework can be used to determine observability for measured, rather than simulated, trajectories. **c.** Same as Figure 4c but for experimental data from the trajectory in **b**. As in Figure 4c, the clear benefit of the AI-UKF is its robustness to different initial conditions and faster convergence to correct estimates.

able to handle these instances without issue (Figure 4f). For very small or zero accelerations the UKF and AI-UKF were equivalent because there was not enough observability for the augmented data-driven state estimate to have an effect (Figure 4f). Overall, the AI-UKF appears to be most beneficial during periods of medium observability where a UKF might fail.

Lastly, we confirmed that the AI-UKF performs well on real

data. We collected optic flow and acceleration measurements from a quadcopter flying with approximately constant altitude and sporadic decelerations/accelerations, and then computed the observability of the trajectory via BOUNDS (Figure 5a–Figure 5b). We found that we could use the same data-driven altitude estimator trained on simulated trajectories (Figure S6) for the real measurements, and it yielded impressive accuracy (Figure 5c). However, when applying a regular UKF we observed similar results to our simulations, wherein the filtered estimates would sometimes not converge for certain initializations (Figure 5c). In contrast, AI-UKF estimates converged quickly to the true altitude and forward velocity (Figure 5c). For some initializations the AI-UKF converged in seconds whereas the UKF did not converge within the ~ 50 -second trajectory (Figure 5c). Overall, we suggest that in situations with limited or sparse sensor data, like in GPS-denied environments, estimating mission-critical state variables can benefit greatly from the AI-KF framework.

DISCUSSION

We introduced a novel framework “BOUNDS: Bounding Observability for Uncertain Nonlinear Dynamic Systems” for empirically evaluating the observability of individual state variables. BOUNDS can be applied to discover active sensing motifs and design corresponding control strategies for autonomous systems or applied to evaluate data collected from moving organisms or machines. In most cases, active sensing motifs are likely to be turning or changes in ground speed, either of the body, or the sensors themselves. BOUNDS can help reveal exactly which combinations of these movements and measurements improve state estimation along observed trajectories of animals, or planned trajectories of machines. Implementing BOUNDS from scratch can be cumbersome, so we provide a Python package *pybounds* that automates these steps with numerous examples (see Code). We additionally introduced a harmonious framework for leveraging observability information about individual state variables—from BOUNDS—to intelligently filter state estimates. By integrating this idea with traditional Kalman filtering approaches, we showed how data-driven individual state estimates that are weighted by observability can be used to augment and improve state estimation with a framework we call the Augmented Information Kalman Filter. We employed a flying agent model to illustrate the applications of our novel methods, but our general framework is amenable to any system leveraging active sensing for estimation.

Tips and Tricks

BOUNDS has just two primary hyper-parameters, 1) the regularization parameter λ (Eq. 3), and 2) the window size ω over which to analyze the observability. It is best practice to choose λ to be large enough to numerically invert the Fisher information matrix, but small enough to not distort the total information. In general, a good guideline is to choose λ to be less than the smallest nonzero eigenvalue of the Fisher information matrix⁴³. Alternatively, one could symbolically compute the limit in Eq. 3, however, this can be computationally expensive and can yield infinite values corresponding to unobservable state variables. For ω , we recommend choosing

a window size roughly equal to the slowest motif of interest. For higher order systems it may be beneficial to take a more automated approach for discovering motifs using techniques either through methodical search¹⁵, or genetic algorithms, particle swarm optimization, or reinforcement learning⁴⁴. Other practical suggestions for applying our approach are provided in the **Methods**.

Constructability and inclusion of model uncertainty

Our observability framework quantifies the minimum error variance for the value of an initial state variable given *subsequent* measurements, i.e. an error bound on $\hat{x}_{i,k}$ given $\mathbf{Y}_{k:k+\omega}$. In state estimation, we are generally interested in building state estimates given *preceding* measurements, that is, we want to find $\hat{x}_{i,k}$ given $\mathbf{Y}_{k-\omega:k}$. To quantify the error bound for this final state, it would be more accurate to use one of observability's dual principles, namely constructability¹⁹, also referred to as the posterior Cramér Rao bound⁴⁵, or observability of the final state⁴⁶. We chose to analyze observability, rather than the mathematically dual concept of constructability (which analyzes the final state, rather than the initial state¹⁹) because it allowed us to use an initial state perturbation approach for empirically calculating the observability matrix \mathcal{O} . This perturbation approach is efficient, and works seamlessly with non-closed-form models. For the purpose of discovering active sensing motifs, both approaches will provide equivalent insight. In cases where a quantification of the error bounds for the final state is necessary, our calculations of \mathcal{F} can be replaced with an iterative equation that uses a discretized time-varying approximation of the continuous-time dynamics¹⁹. Taking this approach would also allow for the inclusion of non-zero process noise covariance matrix Q to understand how uncertainty of an agent's internal model affects the observability (or constructability) of state variables of interest. We note that for the relatively short time windows and small model covariances ($Q \approx 0$) that we considered, the observability and constructability will generally be strongly correlated, allowing us to use our empirical observability calculations as a proxy for constructability. For our demonstration of the AI-KF we circumvented this issue by empirically establishing the error bound of a data-driven estimator by analyzing its error variance directly.

Limitations and future directions of the AI-KF

One limitation that will need to be addressed in the future is that the AI-KF may artificially shrink error covariances during periods of high observability, particularly if multiple data-driven estimators are used to augment the KF. This could be mitigated by only using augmented information when the AI-KF and UKF disagree, and by carefully considering the covariance of data-driven estimators that have coupled performance (i.e. off diagonals of \mathcal{R}'). We note that the UKF also fails to provide accurate estimates of covariance, particularly during periods of low observability (Fig. 4d), something that future work with observability or constructability metrics may also help to address.

Active sensing in organisms

Perhaps the most critical component to active sensing is knowing *when* to do it. Constantly performing active sensing ma-

neuvers can be wasteful, or may conflict with other navigation goals. To achieve a balance, many animals appear to alternate between these two goals in an exploration vs. exploitation trade-off that is triggered when estimates reach a threshold of error²¹. The observability-informed filter approach we introduced provides a flexible and parsimonious framework for taking advantage of observability information (or an approximation thereof) to intelligently update state estimates only during periods of intermittent active sensing (Figure 3). Whether animals use something resembling an observability filter or AI-KF remains an open question. However, *Drosophila* have been shown to throttle learning plasticity based on a turning signal⁴⁷, a motif that we find generally corresponds to high levels of observability for many state variables (Fig. 2c). In many regions of the brain multiple sensory signals are combined together, often with low- or high-pass filter dynamics, making it difficult to understand what role these signals may play. Our approach can be used to understand which task relevant state variables these multiplexed signals can estimate, thereby providing hypotheses about their role in navigation⁴⁸.

Combining data-driven and model-based estimation in robotics

Model-based state estimation is the standard for autonomous systems²⁴. However, for challenging estimation tasks there are clear advantages to methods that incorporate time windows of sensor information through nonlinear optimization approaches (e.g. wind estimation⁴¹ and monocular SLAM⁴⁹), or more recent data-driven machine learning methods⁵⁰. Such methods, however, rarely confer advantages that traditional methods provide such as stability guarantees and computational simplicity. The AI-KF provides a bridge between these two worlds by outlining a statistically meaningful approach for blending model-based and data-driven estimation. The approach is inherently modular, making it easy for individual data-driven estimators to be added or removed from the AI-KF without requiring retraining or retuning. For example, existing monocular SLAM (Simultaneous Localization and Mapping) estimates⁵¹, or deep visual odometry estimates⁵⁰ can be incorporated into the AI-KF without further modification. We do not suggest that the AI-KF will universally improve upon traditional methods, however its benefits emerge for systems with sparse and dynamic observability properties that are difficult for traditional methods to handle. Together, our BOUNDS and AI-KF methods can help engineers develop machines that use active sensing to minimize the number of required sensors, plan trajectories, and design state estimators that work harmoniously to enable levels of robustness commonly observed in organisms.

METHODS

Observability calculations

Empirical observability matrix

We constructed empirical observability matrices \mathcal{O} as previously described¹³. In brief, for a given state trajectory \mathbf{X} we set a window size ω and initial state \mathbf{x}_0 in sliding windows (Figure 1a). Then we perturbed each individual initial state variable by a small amount $\varepsilon = 1 \times 10^{-5}$ in both directions $x_{i,0}^{\pm} = x_{i,0} \pm \varepsilon$. The resulting differences in the sensor mea-

measurements \mathbf{Y} (Figure 1c) was collected and normalized by the perturbation amount $\Delta \mathbf{Y}/2\varepsilon$ and arranged as rows in \mathcal{O} (Figure 1e). All angular measurement variables were unwrapped to ensure that $\Delta \mathbf{Y}$ did not have any discontinuities, a prerequisite for empirical observability analysis. We set a window size of $\omega = 5$ for all simulations.

Fisher information and its inverse

For each \mathcal{O} we computed the Fisher information matrix as $\mathcal{F} = \mathcal{O}^T \mathcal{R}^{-1} \mathcal{O}$. We set the block diagonal noise covariance matrix $\mathcal{R} = 0.1 \cdot I_{(p \times \omega) \times (p \times \omega)}$ where p is the number of measurements and ω is the sliding window size. This assumes the noise variance on each measurement is either 0.1 rad for angular measurements, 0.1 m s⁻¹ for airspeed and ground speed magnitude measurements, and 0.1 s⁻¹ for optic flow measurements. The absolute noise properties of these measurements do not have a large impact on our results because larger or smaller values of \mathcal{R} simply scale \mathcal{F} , however relative changes in \mathcal{R} for different measurements would have an effect. We do not consider the process noise Q in this manuscript, but with some modifications to our method (see¹⁹) this can be taken into account as well. Process noise will have a relatively small effect for a small window size, so this is a reasonable assumption.

Calculating the inverse of \mathcal{F} is often not straightforward due to the presence of unobservable directions, which results in a matrix that is not invertible. A pseudoinverse can be computed, but this results in misleading (often small, when they should be very large) values within the diagonal elements of \mathcal{F}^{-1} for unobservable state variables. Therefore, we chose to add a small amount of observability to each direction in \mathcal{F} to ensure computing a traditional inverse was possible (Equation 3). We refer to this inverse as the “Chernoff inverse”³⁸, following the naming convention of prior literature on matrix inverses⁵². Note that the regularization does not have to be of the form $\lambda I_{n \times n}$. A more general regularization of λJ , where J is any $n \times n$ positive definite matrix, is allowable. For simplicity, we chose J to be the identity matrix. This method results in a cap on the upper bound of the error noise covariance matrix equal to $1/\lambda$. For all systems, $\lambda I_{n \times n}$ must be carefully selected to ensure that it is small enough not to distort the true observability properties, while still large enough to avoid numerical instabilities associated with computing a numerical inverse. We set $\lambda = 1 \times 10^{-6}$ for all calculations.

Tips and tricks

In general, our method is appropriate for any system, as long as the system can be simulated. However, it is critical to ensure that none of the state variables have discontinuities in the state space of the simulation. Otherwise, artifacts can manifest as extremely large values in the observability matrix, which corrupt the computation of the Fisher information matrix. For instance, when dealing with polar variables, such as angles, it is crucial to ensure that the state perturbations required to construct the observability matrix do not lead to angle wrapping discontinuities. Magnitude variables must not be perturbed to be negative if using central/backwards difference methods to calculate a Jacobian, as magnitudes are defined to always be positive. This would have the same effect in the observability matrix as applying a 180° perturbation to the associated angu-

lar quantity. It is possible, and recommended, to represent a single angular measurement as the sine and cosine components of the unit vector associated with the angle—this can mitigate the chance for wrapping discontinuities. It is also important to ensure that all measurement functions are always defined. If a measurement consists of a fraction such as y_1/y_2 , then $y_2 = 0$ would lead to an undefined measurement which breaks observability assumptions.

When considering the observability associated with many different combinations of sensors, it is best practice to compute the observability matrix once for all the potential state variables and sensors, and for the largest time window to be considered. Then one can pull out smaller observability matrices corresponding to whatever combinations of state variables, sensors, and time windows for further analysis (Fisher information, etc.). This is in contrast to performing many simulations to reconstruct a new observability matrix for each unique combination, which effectively contains the same information. This approach avoids cumbersome computations and makes iterative investigation of active sensing motifs much faster, although this is dependent on the speed of the simulation required to construct the observability matrix.

Flying agent dynamical models

Kinematic model

The primary model employed for observability analysis (see Figure 2) was a 3D kinematic model for a flying agent. We use the word “kinematic” here to describe a model that does not rely on force and torque inputs, but rather inputs that can be measured kinematically, like accelerations and angular rates. We chose to use a kinematic model because it is more agnostic to the diverse range of dynamics of flying agents, and may provide more general conclusions. Although we use a continuous-time model to describe the underlying dynamics, the dynamics were effectively converted to discrete-time when solving the differential equations. The model is defined in state space as

$$\dot{\mathbf{x}} = \begin{bmatrix} \dot{x} \\ \dot{y} \\ \dot{z} \\ \dot{v}_x \\ \dot{v}_y \\ \dot{v}_z \\ \dot{\phi} \\ \dot{\theta} \\ \dot{\psi} \\ \dot{w} \\ \dot{\zeta} \end{bmatrix} = \begin{bmatrix} v_x \cos(\psi) - v_y \sin(\psi) \\ v_x \sin(\psi) + v_y \cos(\psi) \\ v_z \\ u_z k_z \cos(\phi) \sin(\theta) - C a_x + v_y \dot{\psi} \\ -u_z k_z \sin(\phi) - C a_y - v_x \dot{\psi} \\ -u_z k_z \cos(\phi) \cos(\theta) - C v_z + g \\ u_\phi k_\phi \\ u_\theta k_\theta \\ u_\psi k_\psi \\ u_w \\ u_\zeta \end{bmatrix}. \quad (16)$$

The model describes the velocity of the agent in the body-level North-East-Down (NED) coordinate system. $[v_x, v_y]$ define translational velocities in the XY plane that rotate with the agents yaw heading ψ and v_z describes the global Z velocity. Note that the derivatives of $[v_x, v_y]$ include the derivative of the rotating reference frame. The body-level frame was chosen primarily because it simplifies the control of trajectories. The position of the agent $[x, y, z]$ was defined in the global frame to more easily visualize trajectories. In general, the choice of reference frame does not affect observability results and

only serves to simplify some of the intermediate steps in our framework.

The model has four inputs for flight control. The acceleration in the body frame u_z serves to counteract acceleration from gravity g (note: we use the symbol g to refer to ground speed apart from this line). By changing roll ϕ and pitch θ , the agent can redirect u_z and control its velocity vector. The inputs $[u_\phi, u_\theta, u_\psi]$ are angular rates that allow the agent to control roll, pitch, and yaw. Most flying systems use a control allocation⁵³ approach to transform these basic inputs into control commands for individual actuators, like motor or tilter commands. However, this level of detail is unnecessary for the purpose of observability analysis and only serves to complicate the control of the agent. Thus, we do not model the actuation associated with these inputs. We augmented the state vector with motor calibration coefficient states for each input $[k_z, k_\phi, k_\theta, k_\psi]$, which were all set equal to one. These augmented states allowed us to consider cases where the agent did not know part of its input dynamics.

We model drag as proportional to the 2D apparent airflow $[a_x, a_y]$ through a drag coefficient C to allow the ambient wind to influence the acceleration of the agent—note that this is a kinematic drag and not a force. The apparent airflow is defined as

$$\begin{bmatrix} a_x \\ a_y \end{bmatrix} = \begin{bmatrix} v_x - w \cos(\psi - \zeta) \\ v_y + w \sin(\psi - \zeta) \end{bmatrix}, \quad (17)$$

where w is the ambient wind magnitude and ζ is the ambient wind direction in the XY plane (Figure 2b,–Figure 2c). To model time-varying wind, we added inputs to control the ambient wind magnitude u_w and direction u_ζ .

Dynamical model

To test the sensitivity of our observability analysis to modeling choices, we also employed a model with more realistic 3D dynamics⁵⁴ (Figure S2). This model is distinct from the kinematic model described above in that it uses forces and torques as inputs and considers physical parameters like mass m , inertia I_\bullet , and drag forces C_\bullet about each axis. The states remained the same as in Equation 16, but we added states for

angular velocity $[\omega_x, \omega_y, \omega_z]$.

$$\dot{\mathbf{x}} = \begin{bmatrix} \dot{x} \\ \dot{y} \\ \dot{z} \\ \dot{v}_x \\ \dot{v}_y \\ \dot{v}_z \\ \dot{\phi} \\ \dot{\theta} \\ \dot{\psi} \\ \dot{\omega}_x \\ \dot{\omega}_y \\ \dot{\omega}_z \\ \dot{u}_w \\ \dot{u}_\zeta \end{bmatrix} = \begin{bmatrix} v_x \cos(\psi) - v_y \sin(\psi) \\ v_x \sin(\psi) + v_y \cos(\psi) \\ v_z \\ \frac{1}{m}(u_z \cos(\phi) \sin(\theta) - C a_x) + v_y \dot{\psi} \\ \frac{1}{m}(-u_z \sin(\phi) - C a_y) - v_x \dot{\psi} \\ \frac{1}{m}(-u_z \cos(\phi) \cos(\theta) - C v_z + m g) \\ \omega_x + \tan(\theta)(\omega_y \sin(\phi) + \omega_z \cos(\phi)) \\ \omega_y \cos(\phi) - \omega_z \sin(\phi) \\ \omega_y \frac{\sin(\phi)}{\cos(\theta)} - \omega_z \frac{\cos(\phi)}{\cos(\theta)} \\ \frac{u_\phi}{I_x} + \frac{I_y - I_z}{I_x} \omega_y \omega_z \\ \frac{u_\theta}{I_y} + \frac{I_z - I_x}{I_y} \omega_x \omega_z \\ \frac{u_\psi}{I_z} + \frac{I_x - I_y}{I_z} \omega_x \omega_y \\ \dot{u}_w \\ \dot{u}_\zeta \end{bmatrix}. \quad (18)$$

Parameter values were chosen based on those measured or estimated for our physical quadcopter system (Table 1). For observability calculations, we included the mass, inertia, and drag parameters in Table 1 as auxiliary state variables. This allowed us to specifically investigate observability when the agent does not have explicit knowledge of its own parameters.

Parameter	Value
mass (m)	2.529 kg
roll inertia (I_x)	0.040 kg m ²
pitch inertia (I_y)	0.040 kg m ²
yaw inertia (I_z)	0.046 kg m ²
translation damping (C)	0.1 kg s ⁻¹

Table 1. Quadcopter model parameters. All values computed for the physical quadcopter system in Figure 5a.

Measurement model

The measurements of our models were chosen depending on which set of measurements we were investigating (Figure 2). However, all measurements were defined as a function of the state variables, and chosen from the set

$$\mathbf{h}(\mathbf{x}) = \begin{bmatrix} \psi \\ \beta \\ \gamma \\ \eta \\ g \\ a \\ r \\ q \end{bmatrix} = \begin{bmatrix} \psi \\ \text{atan2}(v_y, v_x) \\ \text{atan2}(a_y, a_x) \\ \text{atan2}(\dot{v}_y, \dot{v}_x) \\ \sqrt{v_x^2 + v_y^2} \\ \sqrt{a_x^2 + a_y^2} \\ g/z \\ \sqrt{(\dot{v}_x - v_y \dot{\psi})^2 + (\dot{v}_y + v_x \dot{\psi})^2} \end{bmatrix}. \quad (19)$$

The $-v_y\dot{\psi}$ and $+v_x\dot{\psi}$ terms are present to cancel out the terms from 18 that describe the derivative of the rotating reference frame, as a body mounted accelerometer would not pick up these terms.

Simulation and control

We simulated our model in Python with a nonlinear differential equation solver⁵⁵. Even though our model was defined with continuous-time dynamics, we simulated each time step discretely with constant inputs for each step. This was done as opposed to interpolating inputs between time steps, as interpolation between steps can cause issues reproducing simulations starting from an arbitrary point along a trajectory due to the way numerical solvers operate. Our discrete time approach ensured that we could start from any given point along a trajectory and maintain the exact simulation thereafter, which was necessary to construct observability matrices in sliding windows.

We used model predictive control (MPC) with full state feedback to precisely control flight trajectories through our model (Equation 18) (Figure 1b). In principle, other control methods could work, but MPC is a good general choice for controlling nonlinear systems. We first prescribed—or took from measured trajectories—a desired set-point for v_x , v_y , and ψ over time (Figure 1a), then used an open-source MPC toolbox⁵⁵ to find the optimal control inputs to track the set-point variables. Our MPC cost function penalized the squared error between each of our set-point series while adding an additional penalty for each control input to ensure more smoother force and torque inputs. Specifics can be found in our publicly available code.

Artificial neural networks

Wind direction estimator

We designed a feed-forward artificial neural network (ANN) for regression to estimate wind direction Figure 3a. There were 12 input neurons consisting of the heading ψ , apparent airflow angle γ , and optic flow angle β in the time window $\omega = 4$. We used three hidden layers with 64 neurons and an output layer with a single neuron to estimate wind direction ζ . All neurons were fully connected and used a rectified linear unit activation function, except for the output layer, which used a linear activation function. We also added a Gaussian noise layer after the input layer ($\mu = 0$, $\sigma = 0.01$ rad), which was only active during training, to help the ANN deal with noise in the measurements. We built and trained our network using TensorFlow⁵⁶ and Keras⁵⁷. We designed a custom loss function to deal with the circular nature of the output variable:

$$f(\zeta, \check{\zeta}) = (\sin(\zeta) - \sin(\check{\zeta}))^2 + (\cos(\zeta) - \cos(\check{\zeta}))^2,$$

where ζ is the true wind direction of the training data and $\check{\zeta}$ is the ANN output (predicted ζ). This function penalizes the squared error between the sine and cosine components of ζ and $\check{\zeta}$.

We generated a dataset of 40,000 simulated trajectories to train and test the wind direction estimator ANN (Figure 3b). We ensured that our dataset consisted of a diversity of trajectory types by randomly choosing parameters from a uniform

distribution between a set range of values for each of the following properties

$$\begin{aligned} w &= [0, 2] \\ \zeta &= [-\pi, \pi] \\ \psi &= [-\pi, \pi] \\ \dot{\psi} &= [-0.11, 0.11] \\ \ddot{\psi} &= [-2.08, 2.08] \\ v_x &= [0.05, 5] \\ v_{x,\omega}/v_{x,0} &= [0.05, 2.0] \\ v_y &= [-0.2, 0.2] \\ \dot{v}_y &= [-0.1, 0.1], \end{aligned}$$

where $v_{x,\omega}/v_{x,0}$ represents an acceleration as the ratio of initial and final v_x . This was used instead of \dot{v}_x to ensure flight was always generally directed forward and there was not backwards flight for small starting v_x values. We applied a 80-20 train-test split to the data. Each trajectory was 0.2 s (21 discrete points). We augmented the measurements from each trajectory with $\omega = 4$ prior time steps, so only the 17 points with ω prior points available were used in training/testing. The training and testing data split into equally sized bins, once sorted by observability and once sorted randomly (Figure 3c). We trained and tested multiple ANN's on these binned datasets (Figure S4). We trained each ANN for 10000 epochs with a batch size of 4096. Specific details can be found in our publicly available code.

Altitude estimator

The altitude estimator ANN was designed similarly to the wind direction estimator ANN (Figure S6a). The ANN had 40 input neurons consisting of the forward optic flow r_x and forward acceleration \dot{v}_z in the time window $\omega = 20$. Like the wind direction estimator, We used three hidden layers with 64 neurons and an output layer with a single neuron to estimate altitude ζ .

We generated a dataset of 2,000 simulated trajectories to train and test the altitude estimator ANN. Each trajectory had a constant altitude between 0 and 20 meters chosen randomly from a uniform distribution. To generate a wide range of forward accelerations, we varied the forward velocity via a sum-of-sines signal with frequency components between 0.1 and 0.9 Hz, amplitudes between -15 and 15 ms^{-1} , phase between $-\pi/2$ and $\pi/2$, and an offset between -10 and 10 ms^{-1} . We applied a 80-20 train-test split to the data. Each trajectory was 11 s (111 discrete points). We augmented the measurements from each trajectory with $\omega = 20$ prior time steps, so only the 91 points with ω prior points available were used in training/testing.

Augmented Information Kalman Filter

We used the MATLAB implementation of an Unscented Kalman Filter (which uses the utilize square-root factorization of covariance matrices for improved numerical stability)³⁰ for all Augmented Information Kalman Filter simulations. The Unscented transform parameters were set to $\alpha = 10^{-3}$, $\beta = 1$, $\kappa = 0$. The initial state and covariance estimates, process noise covariance, and measurement noise were varied (Figure 4). The baseline noise variance for the

optic flow measurement was set to 10^{-3} . Specifics can be found in our publicly available code.

Outdoor experiments

We collected data from a quadcopter (DJI Matrice 300 RTK) flying outdoors in an open, grassy park area with relatively flat terrain near Reno, NV (Figure 5a). Acceleration data was measured by the onboard accelerometer and ventral camera images were collected at 60 Hz by a ventrally mounted Raspberry Pi camera. Optic flow was computed offline using an implementation of Dense Inverse Search in OpenCV (Python) and low-pass filtered with a cutoff frequency of 1 Hz⁵⁸. We scaled the optic flow with a constant scalar (approximately 0.057) to account for camera and lens properties such that optic flow was equivalent to the ratio of velocity over altitude. Ground truth data was measured by an onboard GPS. All flights were operated in velocity control mode, with manually specified accelerations/decelerations.

DATA AND CODE AVAILABILITY

We provide a Python package to implement BOUNDS (<https://github.com/vanbreugel-lab/pybounds>) which will be updated periodically. Specific data associated with this manuscript will be made public upon publication.

FUNDING

This work was supported by a National Science Postdoctoral Fellowship in Biology to Benjamin Cellini (NSF 22-623). The work was also supported by the Air Force Office of Scientific Research (FA9550-21-0122) to FvB, the NSF AI institute in Dynamics (2112085) to FvB, NSF-EFRI-BRAID (2318081) to FvB, Sloan Research Fellowship (FG-2020-13422) to FvB, and DEPSCoR (FA9950-23-1-0483) to FvB. This research was also supported in part by the NSF grant PHY-2309135 to the Kavli Institute for Theoretical Physics (KITP), which supported valuable discussions that led to substantial improvements of the paper. For the purpose of open access, the author has applied a CC BY public copyright license to any Author Accepted Manuscript version arising from this submission.

ACKNOWLEDGMENTS

We thank Christina May for productive conversations about applications of observability analysis on real data and feedback on *pybounds* code, Stanley David Stupski for providing data for testing, and J. Humberto Ramos for help developing the quadcopter dynamical model.

CONFLICTS OF INTEREST

The authors declare no conflict of interest.

AUTHOR CONTRIBUTIONS

Conceptualization: B.C, B.B, F.v.B.; Methodology: B.C, B.B, A.L, F.v.B.; Software: B.C; Formal analysis: B.C; Investigation: B.C, F.v.B.; Resources: F.v.B.; Data curation: B.C, A.L; Writing - original draft: B.C, F.v.B.; Writing - review & editing: B.C, B.B, A.L, F.v.B.; Visualization: B.C, F.v.B.; Supervision: F.v.B.; Project administration: F.v.B.; Funding acquisition: B.C, F.v.B.;

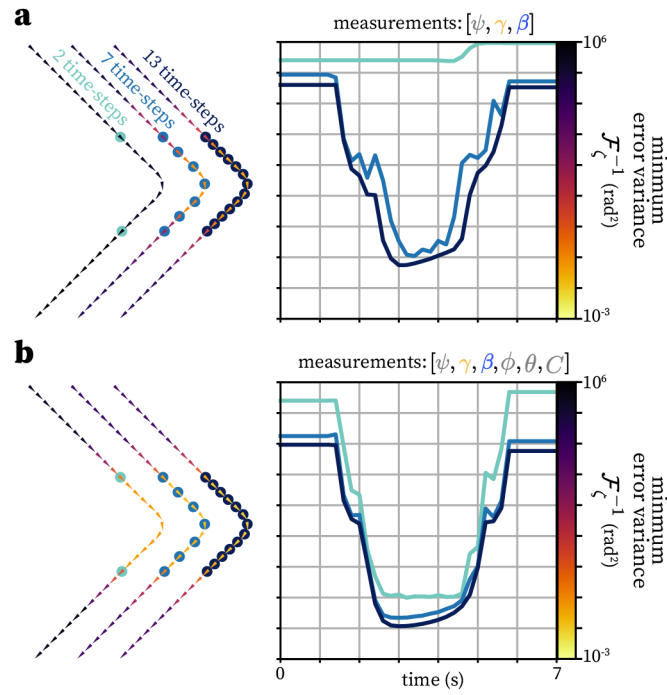
REFERENCES

- [1] Agostino Martinelli. Observability properties and deterministic algorithms in visual-inertial structure from motion. *Foundations and Trends in Robotics*, 3(3):139–209, 2012. doi:[10.1561/23000000030](https://doi.org/10.1561/23000000030).
- [2] Floris van Breugel and Michael H. Dickinson. Plume-Tracking Behavior of Flying *Drosophila* Emerges from a Set of Distinct Sensory-Motor Reflexes. *Current Biology*, 24(3):274–286, feb 2014. doi:[10.1016/j.cub.2013.12.023](https://doi.org/10.1016/j.cub.2013.12.023).
- [3] Floris van Breugel, Kristi Morgansen, and Michael H. Dickinson. Monocular distance estimation from optic flow during active landing maneuvers. *Bioinspiration & Biomimetics*, 9(2):025002, may 2014. doi:[10.1088/1748-3182/9/2/025002](https://doi.org/10.1088/1748-3182/9/2/025002).
- [4] Bryson Lingenfelter, Arunava Nag, and Floris van Breugel. Insect inspired vision-based velocity estimation through spatial pooling of optic flow during linear motion. *Bioinspiration & Biomimetics*, 2021. doi:[10.1088/1748-3190/ac1f7b](https://doi.org/10.1088/1748-3190/ac1f7b).
- [5] Philip RL Parker, Elliott TT Abe, Natalie T Beatie, et al. Distance estimation from monocular cues in an ethological visuomotor task. *eLife*, 11:e74708, sep 2022. doi:[10.7554/eLife.74708](https://doi.org/10.7554/eLife.74708).
- [6] Michael Poteser and Karl Kral. Visual distance discrimination between stationary targets in praying mantis: an index of the use of motion parallax. *Journal of Experimental Biology*, 198(10):2127–2137, October 1995. doi:[10.1242/jeb.198.10.2127](https://doi.org/10.1242/jeb.198.10.2127).
- [7] Robert Hermann and Arthur Krener. Nonlinear controllability and observability. *IEEE Transactions on automatic control*, 22(5):728–740, 2003.
- [8] Floris van Breugel. A nonlinear observability analysis of ambient wind estimation with uncalibrated sensors, inspired by insect neural encoding. In *60th IEEE Conf. on Decision and Control*, pages 1399–1406, 2021. doi:[10.1109/CDC45484.2021.9683219](https://doi.org/10.1109/CDC45484.2021.9683219).
- [9] Milena Anguelova. *Nonlinear Observability and Identifiability: General Theory and a Case Study of a Kinetic Model for S. cerevisiae*. PhD thesis, Chalmers University of Technology and Göteborg University, 2004.
- [10] Antonio J Marques. On the relative observability of a linear system. Master’s thesis, Naval Postgraduate School, 1986.
- [11] Long Rui, Qin Yong-yuan, and Jia Ji-chao. Observable degree analysis of SINS initial alignment based on singular value decomposition. In *IEEE Int. Symposium on Knowledge Acquisition and Modeling Workshop*, pages 444–448, 2008. doi:[10.1109/KAMW.2008.4810520](https://doi.org/10.1109/KAMW.2008.4810520).
- [12] Arthur J. Krener and Kayo Ide. Measures of unobservability. In *Proceedings of the 48th IEEE Conference on Decision and Control (CDC) held jointly with 2009 28th Chinese Control Conference*, pages 6401–6406. IEEE, dec 2009. doi:[10.1109/CDC.2009.5400067](https://doi.org/10.1109/CDC.2009.5400067).
- [13] Benjamin Cellini, Burak Boyacıoğlu, Floris van Breugel, et al. Empirical Individual State Observability. *2023 62nd IEEE Conference on Decision and Control (CDC)*, pages 8450–8456, dec 2023. doi:[10.1109/CDC49753.2023.10383812](https://doi.org/10.1109/CDC49753.2023.10383812).

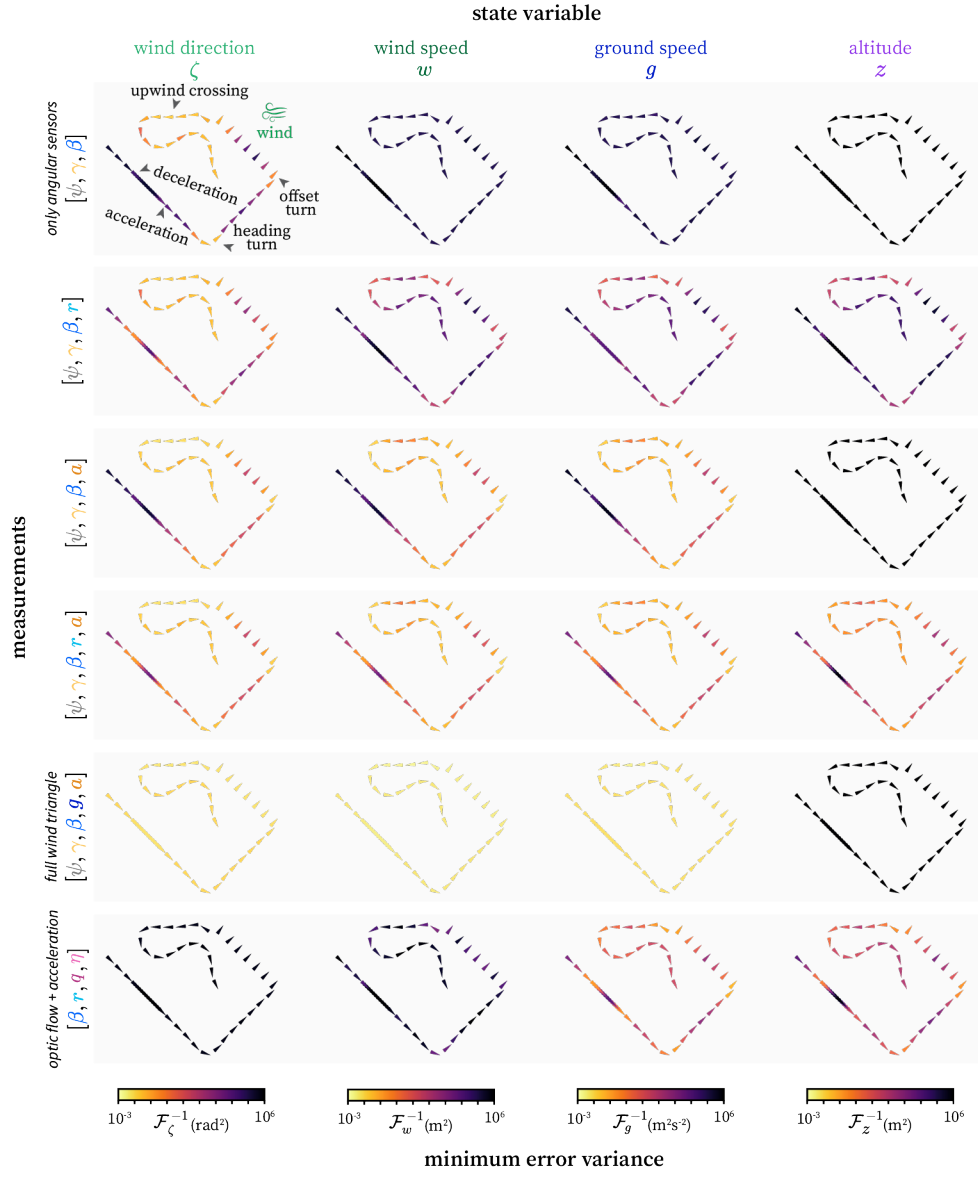
- [14] Pierre-François Massiani, Mona Buisson-Fenet, Friedrich Solowjow, et al. Data-Driven Observability Analysis for Nonlinear Stochastic Systems. *IEEE Transactions on Automatic Control*, 69(6):4042–4049, jun 2024. doi:[10.1109/TAC.2023.3346812](https://doi.org/10.1109/TAC.2023.3346812).
- [15] Benjamin Cellini, Burak Boyacıoğlu, Stanley David Stupski, and Floris van Breugel. Discovering and exploiting active sensing motifs for estimation with empirical observability. *bioRxiv*, pages 2024–11, 2024.
- [16] Sanjay Lall, Jerrold E Marsden, and Sonja Glavaški. Empirical model reduction of controlled nonlinear systems. *IFAC Proceedings Volumes*, 32(2):2598–2603, jul 1999. doi:[10.1016/s1474-6670\(17\)56442-3](https://doi.org/10.1016/s1474-6670(17)56442-3).
- [17] Max Schwenzer, Muzaffer Ay, Thomas Bergs, and Dirk Abel. Review on model predictive control: An engineering perspective. *The International Journal of Advanced Manufacturing Technology*, 117(5):1327–1349, 2021.
- [18] James O. Berger. *Statistical Decision Theory and Bayesian Analysis*. Springer Series in Statistics. Springer New York, New York, NY, 1985. doi:[10.1007/978-1-4757-4286-2](https://doi.org/10.1007/978-1-4757-4286-2).
- [19] Burak Boyacıoğlu and Floris van Breugel. Duality of Stochastic Observability and Constructability and Links to Fisher Information. *IEEE Control Systems Letters*, 8: 3458–3463, 2024. doi:[10.1109/LCSYS.2025.3547297](https://doi.org/10.1109/LCSYS.2025.3547297).
- [20] Harald Cramér. *Mathematical Methods of Statistics*. Princeton Univ. Press, Princeton, NJ, 1946.
- [21] Debojyoti Biswas, Andrew Lamperski, Yu Yang, et al. Mode switching in organisms for solving explore-versus-exploit problems. *Nature Machine Intelligence*, 2023. doi:[10.1038/s42256-023-00745-y](https://doi.org/10.1038/s42256-023-00745-y).
- [22] Osman Kaan Karagoz, Aysegul Kilic, Emin Yusuf Aydin, et al. Predictive uncertainty in state-estimation drives active sensing. *Bioinspiration & Biomimetics*, 20(1): 016018, dec 2024. doi:[10.1088/1748-3190/ad9534](https://doi.org/10.1088/1748-3190/ad9534).
- [23] J. Humberto Ramos, Davis W. Adams, Kevin M. Brink, and Manoranjan Majji. Observability Informed Partial-Update Schmidt Kalman Filter. In *2021 IEEE 24th International Conference on Information Fusion (FUSION)*, pages 1–8. IEEE, nov 2021. doi:[10.23919/FUSION49465.2021.9626946](https://doi.org/10.23919/FUSION49465.2021.9626946).
- [24] Claudio Urrea and Rayko Agramonte. Kalman filter: historical overview and review of its use in robotics 60 years after its creation. *Journal of Sensors*, 2021(1): 9674015, 2021.
- [25] Eric A. Butcher, Jingwei Wang, and T. Alan Lovell. On Kalman Filtering and Observability in Nonlinear Sequential Relative Orbit Estimation. *Journal of Guidance, Control, and Dynamics*, 40(9):2167–2182, sep 2017. doi:[10.2514/1.G002702](https://doi.org/10.2514/1.G002702).
- [26] Marc Bocquet, Karthik S. Gurumoorthy, Amit Apte, et al. Degenerate Kalman Filter Error Covariances and Their Convergence onto the Unstable Subspace. *SIAM/ASA Journal on Uncertainty Quantification*, 5(1):304–333, jan 2017. doi:[10.1137/16M1068712](https://doi.org/10.1137/16M1068712).
- [27] Thijs Devos, Matteo Kirchner, Jan Croes, et al. Sensor Selection and State Estimation for Unobservable and Non-Linear System Models. *Sensors*, 21(22):7492, nov 2021. doi:[10.3390/s21227492](https://doi.org/10.3390/s21227492).
- [28] Simon J Julier and Jeffrey K Uhlmann. New extension of the kalman filter to nonlinear systems. In *Signal processing, sensor fusion, and target recognition VI*, volume 3068, pages 182–193. Spie, 1997.
- [29] Eric A Wan and Rudolph Van Der Merwe. The unscented kalman filter for nonlinear estimation. In *Proceedings of the IEEE 2000 adaptive systems for signal processing, communications, and control symposium (Cat. No. 00EX373)*, pages 153–158. Ieee, 2000.
- [30] E.A. Wan and R. Van Der Merwe. The unscented Kalman filter for nonlinear estimation. In *Proceedings of the IEEE 2000 Adaptive Systems for Signal Processing, Communications, and Control Symposium (Cat. No.00EX373)*, volume 31, pages 153–158. IEEE, 2006. doi:[10.1109/ASSPCC.2000.882463](https://doi.org/10.1109/ASSPCC.2000.882463).
- [31] Abhay K. Singh and Juergen Hahn. On the use of empirical gramians for controllability and observability analysis. *Proceedings of the American Control Conference*, 1 (May):140–141, 2005. doi:[10.1109/acc.2005.1469922](https://doi.org/10.1109/acc.2005.1469922).
- [32] Roman Vaxenburg, Igor Siwanowicz, Josh Merel, et al. Realistic physics simulation of fruit fly locomotion with reinforcement learning. *arXiv preprint*, 2024.
- [33] Burak Boyacıoğlu, Mahnoush Babaei, Amanuel H. Mamo, et al. Sensor Placement for Flapping Wing Model Using Stochastic Observability Gramians. In *2024 American Control Conference (ACC)*, pages 4960–4966. IEEE, jul 2024. doi:[10.23919/ACC60939.2024.10644510](https://doi.org/10.23919/ACC60939.2024.10644510).
- [34] E. F. Camacho and C. Bordons. *Model Predictive control*. Advanced Textbooks in Control and Signal Processing. Springer London, London, 2007. doi:[10.1007/978-0-85729-398-5](https://doi.org/10.1007/978-0-85729-398-5).
- [35] Didier Georges. Towards Optimal Architectures for Hazard Monitoring Based on Sensor Networks and Crowdsensing. *IDRiM Journal*, 10(1):69–111, nov 2020. doi:[10.5595/001c.17963](https://doi.org/10.5595/001c.17963).
- [36] Chun Sik Hwang. *Observability and Information Structure of Nonlinear Systems*,. PhD thesis, Oregon State University, 1985.
- [37] Claude Jauffret. Observability and fisher information matrix in nonlinear regression. *IEEE Transactions on Aerospace and Electronic Systems*, 43(2):756–759, apr 2007. doi:[10.1109/TAES.2007.4285368](https://doi.org/10.1109/TAES.2007.4285368).
- [38] Herman Chernoff. Locally optimal designs for estimating parameters. *The Annals of Mathematical Statistics*, pages 586–602, 1953.
- [39] R. Penrose. A generalized inverse for matrices. *Mathematical Proceedings of the Cambridge Philosophical Society*, 51(3):406–413, jul 1955. doi:[10.1017/S0305004100030401](https://doi.org/10.1017/S0305004100030401).
- [40] Harry L. Van Trees. *Detection, Estimation, and Modulation Theory, Part I*. John Wiley & Sons, Inc., New York, USA, sep 2001. doi:[10.1002/0471221082](https://doi.org/10.1002/0471221082).
- [41] Floris van Breugel, Renan Jewell, and Jaleesa Houle. Active anemosensing hypothesis: how flying insects could estimate ambient wind direction through sensory integration and active movement. *Journal of The Royal Society Interface*, 19(193):2022.03.31.486300, aug 2022. doi:[10.1098/rsif.2022.0258](https://doi.org/10.1098/rsif.2022.0258).
- [42] Martin Brossard, Axel Barrau, and Silvere Bonnabel.

- AI-IMU Dead-Reckoning. *IEEE Transactions on Intelligent Vehicles*, 5(4):585–595, dec 2020. doi:[10.1109/TIV.2020.2980758](https://doi.org/10.1109/TIV.2020.2980758).
- [43] Roger A. Horn and Charles R. Johnson. *Matrix Analysis*. Cambridge University Press, oct 2012. doi:[10.1017/CBO9781139020411](https://doi.org/10.1017/CBO9781139020411).
- [44] J. Kennedy and R. Eberhart. Particle swarm optimization. In *Proceedings of ICNN'95 - International Conference on Neural Networks*, volume 4, pages 1942–1948. IEEE, 1995. doi:[10.1109/ICNN.1995.488968](https://doi.org/10.1109/ICNN.1995.488968).
- [45] Petr Tichavsky, Carlos H Muravchik, and Arye Nehorai. Posterior cramer-rao bounds for discrete-time nonlinear filtering. *IEEE Transactions on signal processing*, 46(5): 1386–1396, 1998.
- [46] Eduardo D. Sontag. *Mathematical Control Theory: Deterministic Finite Dimensional Systems*. Springer-Verlag, 1 edition, 1990.
- [47] Yvette E. Fisher, Michael Marquis, Isabel D’Alessandro, and Rachel I. Wilson. Dopamine promotes head direction plasticity during orienting movements. *Nature*, 612 (7939):316–322, dec 2022. doi:[10.1038/s41586-022-05485-4](https://doi.org/10.1038/s41586-022-05485-4).
- [48] Christina E May, Benjamin Cellini, Floris van Breugel, and Katherine I Nagel. A compact multisensory representation of self-motion is sufficient for computing an external world variable. *bioRxiv*, pages 2025–05, 2025.
- [49] Shaojie Shen, Nathan Michael, and Vijay Kumar. Tightly-coupled monocular visual-inertial fusion for autonomous flight of rotorcraft mavs. In *2015 IEEE International Conference on Robotics and Automation (ICRA)*, pages 5303–5310, 2015. doi:[10.1109/ICRA.2015.7139939](https://doi.org/10.1109/ICRA.2015.7139939).
- [50] Roberto Pellerito, Marco Cannici, Daniel Gehrig, et al. Deep visual odometry with events and frames. In *2024 IEEE/RSJ International Conference on Intelligent Robots and Systems (IROS)*, pages 8966–8973. IEEE, 2024.
- [51] Stephan Weiss, Davide Scaramuzza, and Roland Siegwart. Monocular-slam-based navigation for autonomous micro helicopters in gps-denied environments. *Journal of Field Robotics*, 28(6):854–874, October 2011. doi:[10.1002/rob.20412](https://doi.org/10.1002/rob.20412).
- [52] C Radhakrishna Rao, Sujit Kumar Mitra, et al. Generalized inverse of a matrix and its applications. In *Proceedings of the sixth Berkeley symposium on mathematical statistics and probability*, volume 1, pages 601–620. University of California Press Oakland, CA, USA, 1972.
- [53] Tor A. Johansen and Thor I. Fossen. Control allocation—A survey. *Automatica*, 49(5):1087–1103, may 2013. doi:[10.1016/j.automatica.2013.01.035](https://doi.org/10.1016/j.automatica.2013.01.035).
- [54] Randal W Beard. Quadrotor Dynamics and Control. *Researchgate.Net*, pages 1–47, 2008.
- [55] Felix Fiedler, Benjamin Karg, Lukas Lüken, et al. dompc: Towards FAIR nonlinear and robust model predictive control. *Control Engineering Practice*, 140:105676, nov 2023. doi:[10.1016/j.conengprac.2023.105676](https://doi.org/10.1016/j.conengprac.2023.105676).
- [56] Martín Abadi, Paul Barham, Jianmin Chen, et al. TensorFlow: A system for large-scale machine learning. *arXiv*, may 2016. doi:<https://doi.org/10.48550/arXiv.1605.08695>.
- [57] François and others Chollet. Keras, 2015.
- [58] G. Bradski. The OpenCV Library. *Dr. Dobb’s Journal of Software Tools*, 2000.

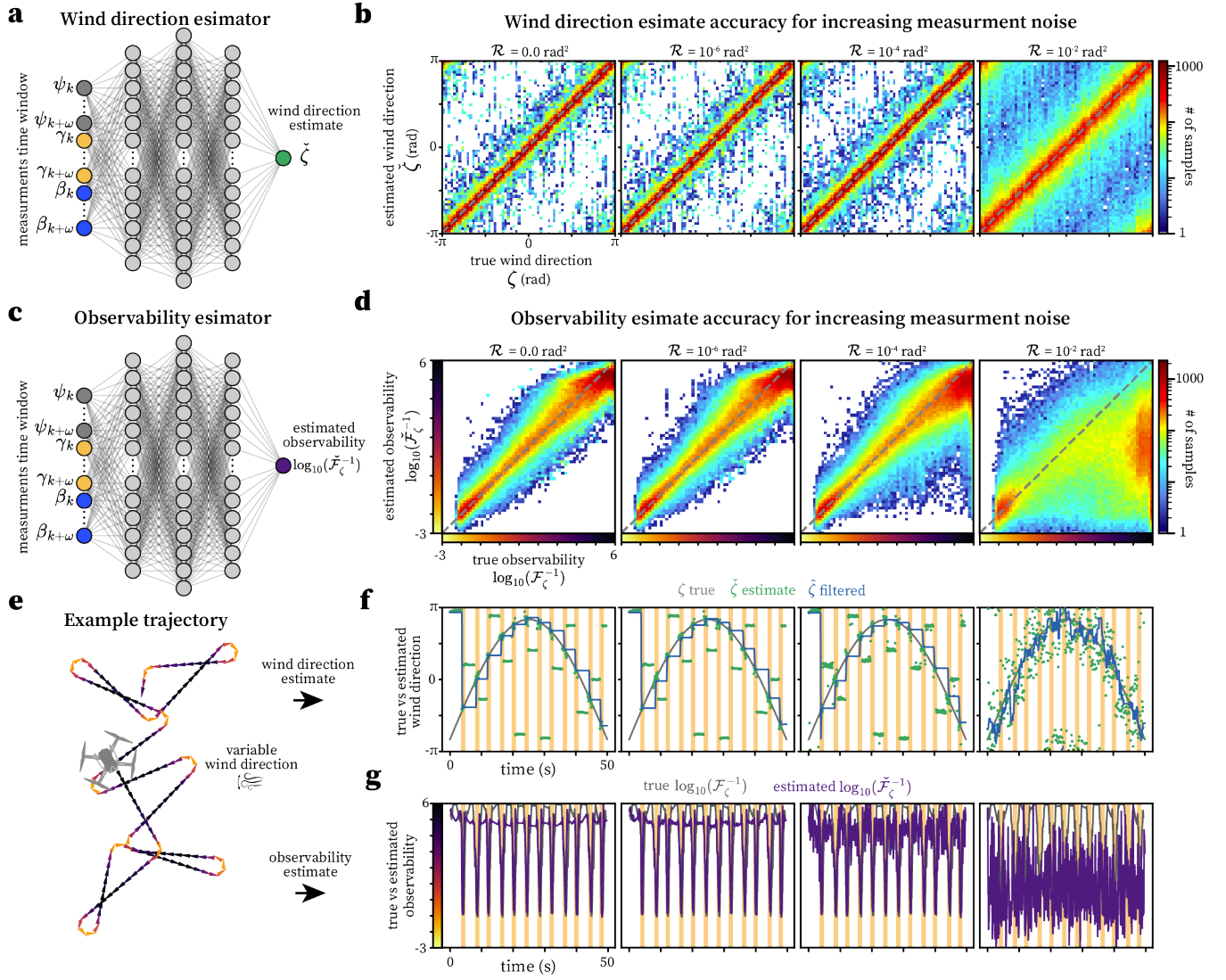
SUPPLEMENTARY MATERIAL



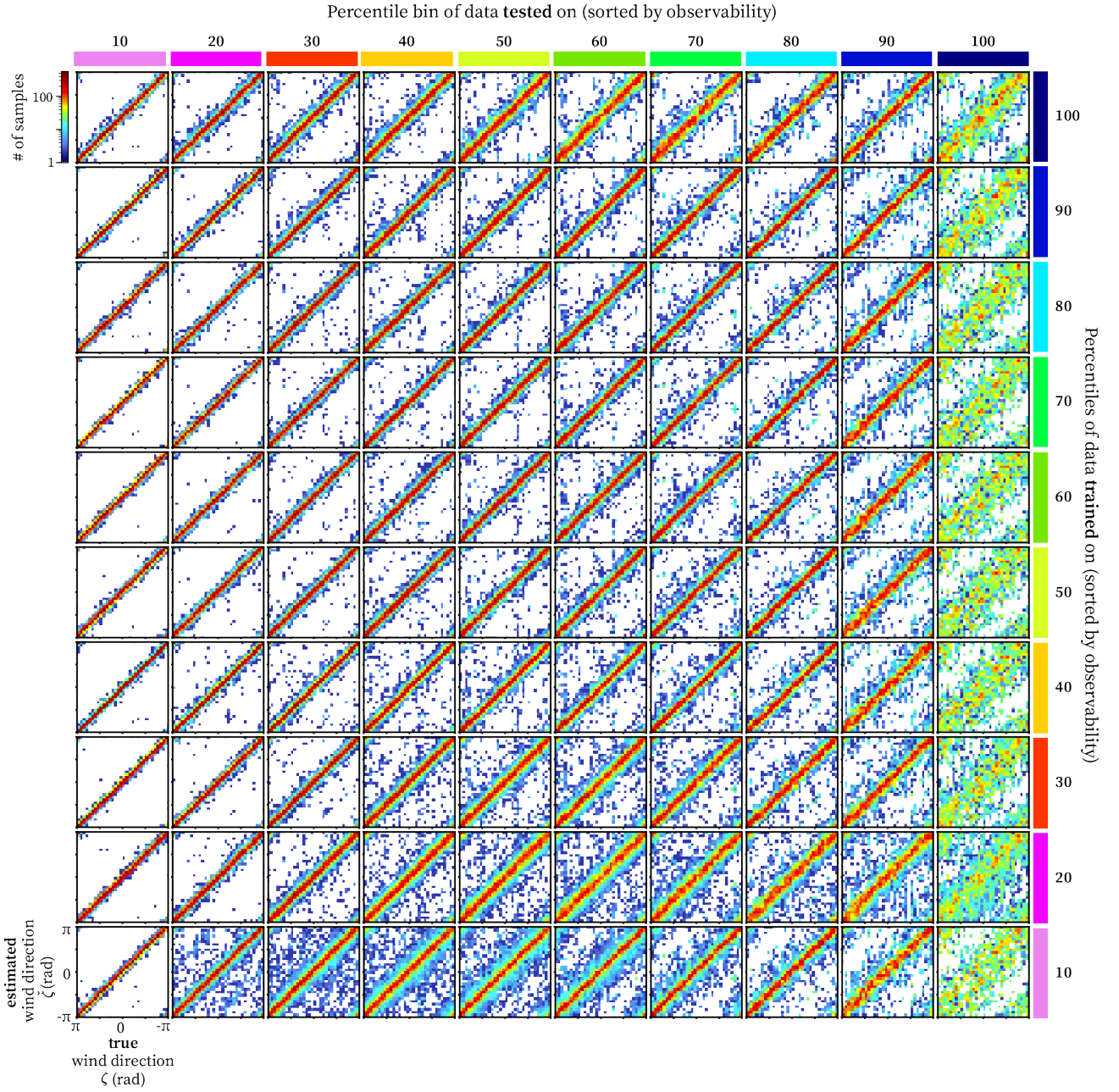
Supplementary Figure S1. Observability for measurements at different times during an active sensing motif. a. The observability of wind direction (calculated as in Figure 2) for the same trajectory, but considering measurements of heading (ψ), course direction (β) and apparent airflow angle (γ) only at specific times during the heading turn. Note that the turn does not increase observability when only considering measurement time steps before and after the turn (green) compared to using time steps throughout the turn (blues). **b.** Same as **a** but with extra measurements of the agent's roll angle (ϕ), pitch angle (θ), and damping translational coefficient (C). Note that this set of measurements enables only two measurement time steps, before and after the turn, to increase observability.



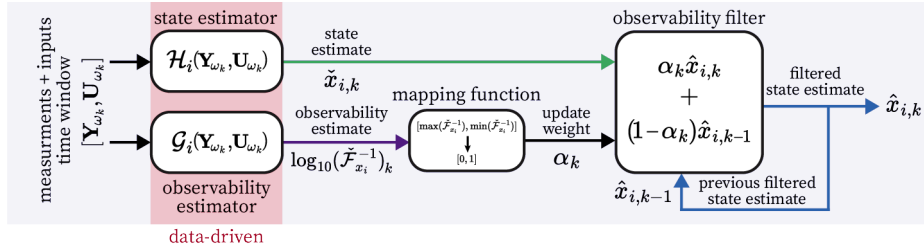
Supplementary Figure S2. Active sensing motifs with a full dynamical drone model. Same as Figure 2 but using a dynamical model.



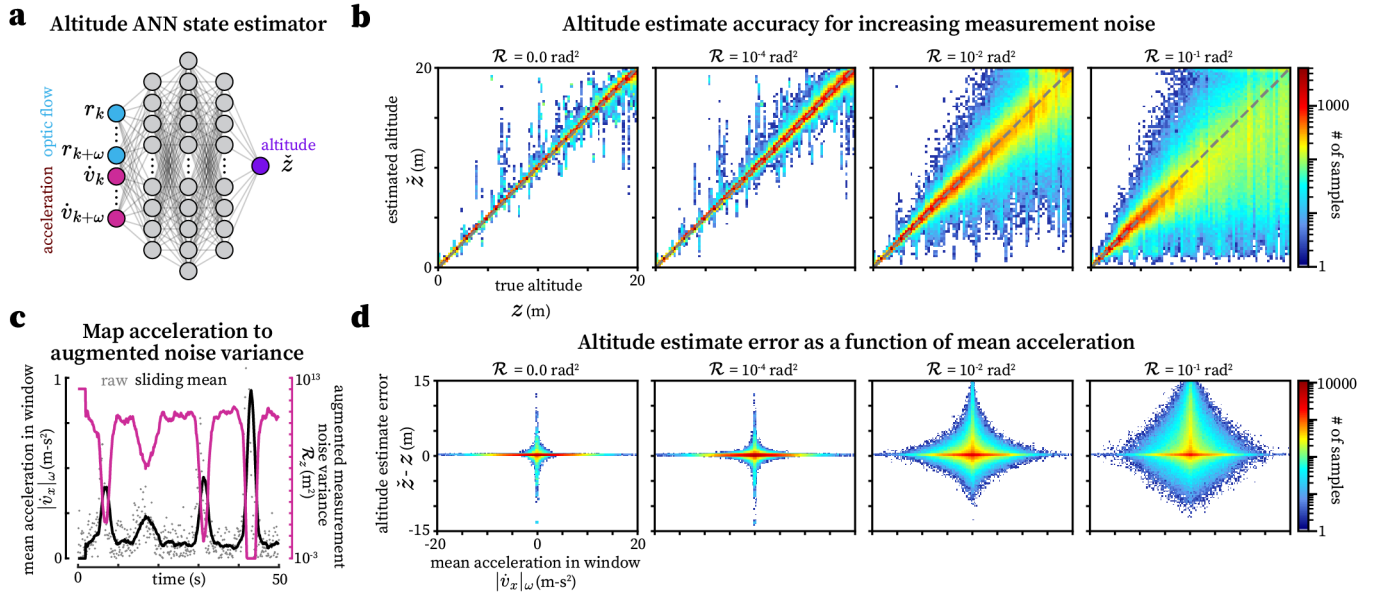
Supplementary Figure S3. ANN Wind direction and wind direction observability estimator performance for varying measurement noise levels. **a.** Wind direction artificial neural network (ANN) estimator (same as Figure 3c). **b.** Wind direction ANN estimator testing performance as a function of the input (measurement) noise levels, where $\mathcal{R} = 10^{-4}$ indicates a noise covariance matrix of $\mathcal{R} = 10^{-4} \times I_{p \times p}$ for the ANN inputs. The gray dashed line indicates perfect performance. **c.** Wind direction observability estimator ANN estimator. **d.** Same as **b.** but for the wind direction observability estimator performance. **e.** An example simulated trajectory (same as Figure 3f) with variable wind direction. **f.** The raw wind direction ANN estimate for the trajectory in **e.** (green) vs true wind direction (gray) for varying measurement noise levels. The “observability-filtered” estimate (see Figure S5) is shown in blue. The orange patches indicate the times of the observable turns during the trajectory. **g.** The wind direction observability ANN estimate for the trajectory in **e.** (purple) vs true observability (gray) for varying measurement noise levels.



Supplementary Figure S4. ANN Wind direction estimator performance. Wind direction artificial neural network (ANN) estimator (see Figure 3c) testing performance as a function of training and testing data with different observability levels. The dataset in Figure 3b was split into 10 equally sized bins and an ANN was trained on 80% of the data from each bin. The withheld 20% of each bin was used to evaluate the performance. Figure 3c shows the testing estimation error variance $\text{Var}(\zeta - \hat{\zeta})$ for each bin corresponding to each panel here compared to ANN's trained on randomly split data. The ANN input (measurement) noise variance were all set to 10^{-4} rad, corresponding to a noise covariance of $\mathcal{R} = 10^{-4} \times I_{p \times p}$.



Supplementary Figure S5. Observability-filter. Overview of observability-informed state estimation framework. Artificial neural networks (ANN) estimate a state variable $x_{i,k}$ (\mathcal{H}_i) and its observability $\mathcal{F}_{x_{i,k}}^{-1}$ (\mathcal{G}_i) from available measurements \mathbf{Y}_{ω_k} and \mathbf{U}_{ω_k} inputs in the time window ω . The state estimate $\tilde{x}_{i,k}$ is adaptively filtered based on the estimated observability $\tilde{\mathcal{F}}_{x_{i,k}}^{-1}$ to change more quickly when observability is high.



Supplementary Figure S6. ANN altitude estimator. **a.** Artificial neural network (ANN) that estimates altitude from measurements of forward optic flow (r_x) and forward acceleration (\dot{v}_x) over the time window ω . **b.** Altitude ANN estimator testing performance as a function of the input (measurement) noise levels, where $\mathcal{R} = 10^{-4}$ indicates a noise covariance matrix of $\mathcal{R} = 10^{-4} \times I_{p \times p}$ for the ANN inputs. The gray dashed line indicates perfect performance. **c.** Illustration of mapping the mean forward acceleration (\dot{v}_x) in the window ω to the augmented noise variance $\tilde{\mathcal{R}}_{z,z}$ for the altitude estimate. **d.** Altitude ANN estimator testing performance as a function of the mean forward acceleration (\dot{v}_x) in the window ω , as a function of the input (measurement) noise levels. Note that the shape of the heatmap illustrates the variance of the altitude estimates.